INTERNATIONAL JOURNAL FOR NUMERICAL METHODS IN ENGINEERING

Int. J. Numer. Meth. Engng 2016; **00**:1–41

Published online in Wiley InterScience (www.interscience.wiley.com). DOI: 10.1002/nme

Modeling crack discontinuities without element-partitioning in the extended finite element method

Eric B. Chin[1], Jean B. Lasserre[2] and N. Sukumar[1,*]

[1] *Department of Civil and Environmental Engineering, University of California, Davis, CA 95616, USA*

[2] *LAAS-CNRS and Institute of Mathematics, University of Toulouse, France*

SUMMARY

In this paper, we model crack discontinuities in two-dimensional linear elastic continua using the extended finite element method without the need to partition an enriched element into a collection of triangles or quadrilaterals. For crack modeling in the X-FEM, the standard finite element approximation is enriched with a discontinuous function and the near-tip crack functions. Each element that is fully cut by the crack is decomposed into two simple (convex or nonconvex) polygons, whereas the element that contains the crack tip is treated as a nonconvex polygon. On using Euler's homogeneous function theorem and Stokes's theorem to numerically integrate homogeneous functions on convex and nonconvex polygons, the exact contributions to the stiffness matrix from discontinuous enriched basis functions are computed. For contributions to the stiffness matrix from weakly singular integrals (due to enrichment with asymptotic crack-tip functions), we only require a one-dimensional quadrature rule along the edges of a polygon. Hence, neither element-partitioning on either side of the crack discontinuity nor use of any cubature rule within an enriched element are needed. Structured finite element meshes consisting of rectangular elements, as well as unstructured triangular meshes, are used. We demonstrate the flexibility of the approach and its excellent accuracy in stress intensity factor computations for two-dimensional crack problems. Copyright © 2016 John Wiley & Sons, Ltd.

Received . . .

KEY WORDS: X-FEM, strong discontinuities, numerical integration, Euler's homogeneous function theorem, homogeneous polynomials, weakly singular integrals

*Correspondence to: N. Sukumar, Department of Civil and Environmental Engineering, University of California, One Shields Avenue, Davis, CA 95616, USA. E-mail: nsukumar@ucdavis.edu

Contract/grant sponsor: National Science Foundation; contract/grant number: CMMI-1334783

Prepared using nmeauth.cls *[Version: 2010/05/13 v3.00]*

1. INTRODUCTION

The extended finite element method (X-FEM), which was introduced by Moës et al. [1], allows the modeling of cracks without their explicit inclusion in the finite element mesh. Instead, the crack is represented by enriching the displacement approximation with two sets of functions — a generalized Heaviside function to model the displacement discontinuity along the crack, and four near-tip functions that capture the asymptotic behavior of the displacement field near the crack tip. These enrichments are included in the displacement approximation through the framework of *partition-of-unity* put forth by Melenk and Babuška [2]. Even though the X-FEM greatly simplifies crack modeling, there still remain open issues, challenges, and improvements that need to be made as discussed in Sukumar et al. [3]. In this paper, we target the issue of accurate numerical integration in two-dimensional elastic fracture analyses with the extended finite element method, and present a new approach for the numerical integration of discontinuous and weakly singular functions that does not require element-partitioning in the X-FEM.

Various approaches have been proposed to integrate discontinuous functions in the X-FEM. A straightforward and widely used approach is to partition the subdomain on either side of the discontinuity into triangles for numerical integration [1]. However, element-partitioning complicates code development, can be time-consuming, and can result in a suboptimal number of cubature points. To avoid element-partitioning, many schemes have been devised. Ventura [4] established that an affine discontinuity can be replaced by an equivalent polynomial expression for linear triangles and bilinear quadrilaterals. A similar approach is formulated by Holdych et al. [5], wherein polynomial-precision cubature rules are developed for triangular elements with an affine discontinuity. Recently, Ventura and Benvenuti [6] extended the prior work of Ventura [4] to elements of any order and dimensionality by replacing the affine discontinuity with a regularized version of a discontinuous function. For piecewise affine discontinuities, other methods of integration have been introduced that do not require element-partitioning. Natarajan et al. [7] applied a Schwarz-Christoffel mapping over the continuous subdomains of an element; however, this mapping introduces errors in the numerical integration. Mousavi and Sukumar [8] used a node elimination algorithm to develop an optimized cubature rule for discontinuous polynomials on polygons, which requires solving a system of nonlinear equations. In their approach, monomial basis functions are integrated using a method developed by Lasserre [9] for integrating homogeneous functions over convex polygons. Sudhakar and

Prepared using nmeauth.cls
DOI: 10.1002/nme

Wall [10] applied moment fitting equations with predefined cubature points to construct a cubature rule that is valid for convex and nonconvex domains. While their algorithm is more efficient than element-partitioning, the number of cubature points in each subdomain is not optimal. Despite these recent advances, element-partitioning remains the method-of-choice for integrating discontinuous functions in the X-FEM.

Accurate and efficient numerical integration of discontinuous and weakly singular near-tip functions is also an outstanding issue in the X-FEM. In order to recover optimal rates of convergence, these functions must be accurately integrated. Polynomial approximations of these functions are poor; therefore, integrating with Gauss cubature requires an inordinate number of cubature points. To address this shortcoming, several integral (singularity-canceling) transformations have been proposed to improve integration accuracy of near-tip functions. These methods transform the domain of integration from a triangle to a rectangle to eliminate the singularity from the integrand, and they require the element containing the singularity to be partitioned into conforming triangles. Béchet et al. [11] introduced a series of mappings that improve integration accuracy of weakly singular functions that appear in the X-FEM. Laborde et al. [12] applied the Duffy transformation [13] to weakly singular near-tip functions and noted improvements in cubature accuracy for functions with a r^{-1} singularity. Mousavi and Sukumar [8] used a generalization of the Duffy transformation [14] that was particularly effective for singularities of type $r^{-1/2}$ and r^{-1}. For singularity-canceling methods, Cano and Moreno [15] devise a general methodology to construct a map (obtained as the solution of an ordinary differential equation) that provides efficient cubature on deformed triangles and on singularities of the type $r^{-\alpha}$, where $0 < \alpha < 2$.

In this paper, we apply a method of numerical integration of homogeneous functions recently developed by the authors [16], which draws on previous work by Lasserre [9, 17], to integrate both discontinuous and weakly singular functions in the X-FEM. For brevity, we refer to this approach as the homogeneous numerical integration (HNI) method. Finite elements with constant Jacobian in the isoparametric map (so that the nodal shape functions and their derivatives are polynomials on the physical element) are suitable for the HNI method. This is not a limitation per se since the X-FEM permits complex crack geometries to be captured on simple, structured meshes. The rest of this paper is organized as follows. In Section 2, we present the main theoretical underpinnings of the new scheme to integrate homogeneous functions over polygons. The strong and weak formulations for two-dimensional

Prepared using nmeauth.cls
DOI: 10.1002/nme

fracture are presented in Section 3.1, and the discrete equations in the X-FEM are developed in Section 3.2 with particular emphasis on the structure of the submatrices contained in the element stiffness matrix. The essentials of the domain form of the contour interaction integral to extract the stress intensity factors (SIFs) are presented in Section 3.3, and the nature of the homogeneous functions that appear in the element stiffness matrix are discussed in Section 3.4. Implementation of the HNI scheme for numerical integration of discontinuous and weakly singular functions is treated in Section 4, where we show that it outperforms the generalized Duffy transformation and tensor-product Gauss cubature rules. In Section 5, stress intensity factor computations using the X-FEM for an edge-crack, inclined center-crack, and a doubly-kinked crack are presented. Both *geometric* and *topological* enrichment strategies are considered and comparisons are made to analytical solutions and to reference results obtained using Abaqus$^{\text{TM}}$ 6.13-1 [18]. Finally, in Section 6, we close with some final remarks and the outlook of using HNI in the X-FEM and related Galerkin methods.

2. INTEGRATION OF HOMOGENEOUS FUNCTIONS

Our objective is to compute

$$\int_P f(\boldsymbol{x})\, d\boldsymbol{x},$$

where $f(\boldsymbol{x})$ is a homogeneous function of degree q and P is a two-dimensional convex or non-convex closed polygon. To this end, we begin by introducing Euler's homogeneous function theorem and the generalized Stokes's theorem.

By definition, a positively homogeneous function of degree q satisfies

$$f(\lambda \boldsymbol{x}) = \lambda^q f(\boldsymbol{x}) \tag{1}$$

for all $\boldsymbol{x}$ and where $\lambda > 0$. Euler's homogeneous function theorem [19] states that if $f(\boldsymbol{x})$ is homogeneous, then it also satisfies

$$q f(\boldsymbol{x}) = \nabla f(\boldsymbol{x}) \cdot \boldsymbol{x} \quad \forall \boldsymbol{x} \in \begin{cases} \mathbb{R}^d & \text{if } q \geq 0 \\ \mathbb{R}^d \setminus \{\boldsymbol{0}\} & \text{if } q < 0 \end{cases}. \tag{2}$$

Prepared using nmeauth.cls
DOI: 10.1002/nme

For a scalar-field f and a vector field $\boldsymbol{X}$, we can write the generalized Stokes's theorem (Gauss's divergence theorem) as [20]

$$\int_M \big(\nabla \cdot \boldsymbol{X}(\boldsymbol{x})\big) f(\boldsymbol{x})\ d\boldsymbol{x} + \int_M \nabla f(\boldsymbol{x}) \cdot \boldsymbol{X}(\boldsymbol{x})\, d\boldsymbol{x} = \int_{\partial M} \big(\boldsymbol{X}(\boldsymbol{x}) \cdot \boldsymbol{n}\big) f(\boldsymbol{x})\, d\sigma, \tag{3}$$

where M is a two-dimensional domain that is bounded by ∂M. In (3), $\boldsymbol{n}$ is the unit outward normal to ∂M and $d\sigma$ is the differential length of the parameterized curve σ on ∂M. Choosing $\boldsymbol{X}(\boldsymbol{x}) := \boldsymbol{x}$ (position vector) and applying Euler's homogeneous function theorem (2), (3) simplifies to [17]

$$\int_M f(\boldsymbol{x})\ d\boldsymbol{x} = \frac{1}{2+q} \int_{\partial M} (\boldsymbol{x} \cdot \boldsymbol{n}) f(\boldsymbol{x})\, d\sigma. \tag{4}$$

For our purposes, we consider a closed, simple (convex or nonconvex) polygon $P \subset \mathbb{R}^2$ that is enclosed by ∂P (Figure 1). The boundary ∂P is defined by m one-dimensional line segments, F_i, where $F_i \subset \mathcal{H}_i$, with $\mathcal{H}_i$ being the line $\boldsymbol{a}_i \cdot \boldsymbol{x} = b_i$ for some $\boldsymbol{a}_i$ and b_i $(i = 1, 2, \ldots, m)$. The sign of b_i is determined such that $\boldsymbol{a}_i / \|\boldsymbol{a}_i\|$ is the outward normal to the polygon.

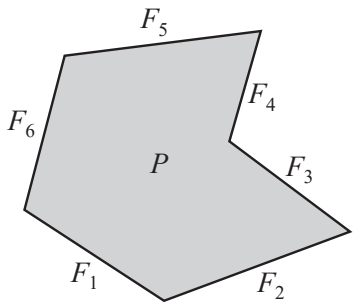

Figure 1. Simple polygon with edges F_i.

With this definition, further simplification are applied to (4). Since we wish to integrate over the polygon, M and ∂M are replaced by P and ∂P, respectively. Additionally, since $F_1 \cup \ldots \cup F_m = \partial P$, integration over ∂P is the same as the sum of the integrals over the line segments. Recognizing that the normal to F_i is $\boldsymbol{n} = \boldsymbol{a}_i / \|\boldsymbol{a}_i\|$, $\boldsymbol{x} \cdot \boldsymbol{n}$ simplifies to $b_i / \|\boldsymbol{a}_i\|$, leaving [16]

$$\int_P f(\boldsymbol{x})\, d\boldsymbol{x} = \frac{1}{2+q} \sum_{i=1}^{m} \frac{b_i}{\|\boldsymbol{a}_i\|} \int_{F_i} f(\boldsymbol{x})\, d\sigma. \tag{5}$$

Note that (5) was restricted to only convex polygons in Reference [9]. The above expression reduces integration over a polygon to integration over its bounding line segments.

Prepared using nmeauth.cls
DOI: 10.1002/nme

If f is a homogeneous polynomial, then on applying (5) recursively, an exact expression for the integral is realized that involves computing f and its partial derivatives at the vertices of the polygon [9]. Alternatively, since Gauss quadrature yields exact integration for polynomials in the interval, here we choose to use Gauss quadrature to compute the line integral in (5). On applying Gauss quadrature, (5) becomes

$$\int_P f(\boldsymbol{x})\, d\boldsymbol{x} = \frac{1}{2+q} \sum_{i=1}^{m} \frac{b_i}{\|\boldsymbol{a}_i\|} \sum_{j=1}^{nq_i} w_{ij} f(\boldsymbol{x}_{ij}).$$

Further, let the index k map to a unique value of i, j and define $\tilde{w}_k \equiv \frac{b_i}{\|\boldsymbol{a}_i\|} w_{ij}$. Then, the nested summation is eliminated and we can write

$$\int_P f(\boldsymbol{x})\, d\boldsymbol{x} = \frac{1}{2+q} \sum_{k=1}^{nq} \tilde{w}_k f(\boldsymbol{x}_k), \tag{6}$$

where nq is the total number of quadrature points.

Finally, consider the integration of $g(\boldsymbol{x})$, defined as a collection of n homogeneous polynomials:

$$g(\boldsymbol{x}) = \sum_{i=1}^{n} f^{[q_i]}(\boldsymbol{x}),$$

where the superscript $[q_i]$ indicates that $f^{[q_i]}$ is a homogeneous polynomial of degree q_i. Applying (6) to $g(\boldsymbol{x})$ yields

$$\int_P g(\boldsymbol{x})\, d\boldsymbol{x} = \sum_{k=1}^{nq} \tilde{w}_k \sum_{i=1}^{n} \frac{1}{2+q_i} f^{[q_i]}(\boldsymbol{x}_k). \tag{7}$$

Note that the sum over the quadrature points appears *outside* the innermost summation in (7). This allows for a single set of quadrature points for the entire integral provided that the quadrature rule is valid for all $f^{[q_i]}(\boldsymbol{x})$ $(i = 1, 2, \ldots, n)$. Equation (7) is an exact cubature rule for a sum of homogeneous polynomials, but in general it is not exact if $f^{[q_i]}(\boldsymbol{x})$ is some other homogeneous function.

With Gauss quadrature applied to the bounding line segments, (6) and (7) provide polynomial-precision numerical integration over arbitrary polygons. In Reference [16], further extensions and generalizations of HNI are detailed; however, (6) and (7) suffice for the remaining developments in this paper.

Prepared using nmeauth.cls
DOI: 10.1002/nme

3. EXTENDED FINITE ELEMENT METHOD

3.1. Strong form and weak form for a crack in linear elastic media

Consider the elastostatic boundary-value problem for a body with a crack that occupies a two-dimensional domain. In the absence of body forces, the strong form is:

$$\begin{aligned} \nabla \cdot \boldsymbol{\sigma} &= \mathbf{0} \text{ in } \Omega, \\ \boldsymbol{u} &= \bar{\boldsymbol{u}} \text{ on } \Gamma_u, \\ \boldsymbol{\sigma} \cdot \boldsymbol{n} &= \bar{\boldsymbol{t}} \text{ on } \Gamma_t, \text{ and} \\ \boldsymbol{\sigma} \cdot \boldsymbol{n} &= \mathbf{0} \text{ on } \Gamma_c, \end{aligned} \tag{8}$$

where $\Omega \subset \mathbb{R}^2$ is the problem domain, $\Gamma = \Gamma_u \cup \Gamma_t \cup \Gamma_c$ is the boundary of Ω with displacement boundary conditions prescribed on Γ_u and traction boundary conditions prescribed on Γ_t (see Figure 2). The traction-free crack domain is Γ_c. In (8), $\boldsymbol{\sigma}$ denotes the Cauchy stress tensor and $\boldsymbol{n}$ is the unit outward normal on the boundary.

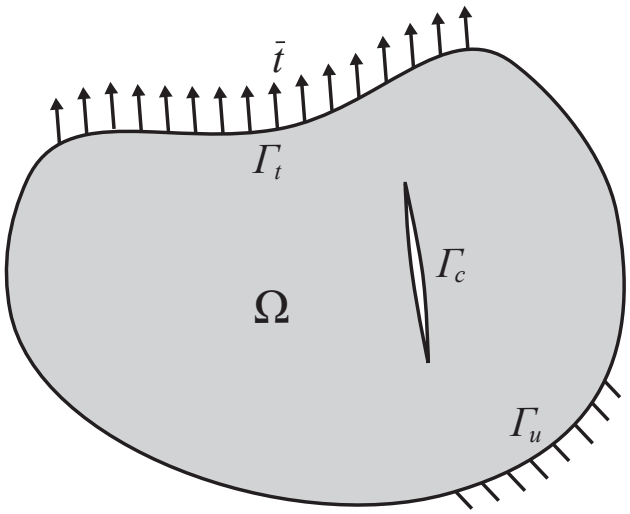

Figure 2. Elastostatic boundary-value problem for an embedded crack.

The HNI method is compatible with any crack Γ_c that can be represented as a union of homogeneous functions (such as algebraic curves). However, for the setting of this paper, we assume that Γ_c is the union of $n_c - 1$ line segments. The i-th line segment is composed of two

Prepared using nmeauth.cls
DOI: 10.1002/nme

vertices: $\boldsymbol{c}_i = (x_i, y_i)$ and $\boldsymbol{c}_{i+1} = (x_{i+1}, y_{i+1})$. The vertices are contained in the matrix

$$\boldsymbol{C} = \begin{bmatrix} \boldsymbol{c}_1 \\ \boldsymbol{c}_2 \\ \vdots \\ \boldsymbol{c}_{n_c} \end{bmatrix}, \tag{9}$$

where the crack tips are given by $\boldsymbol{c}_1$ and/or $\boldsymbol{c}_{n_c}$.

The weak form of (8) is: find $\boldsymbol{u} \in \mathcal{U}$ such that

$$\begin{aligned} &a(\boldsymbol{u}, \delta\boldsymbol{u}) = \ell(\delta\boldsymbol{u}) \quad \forall \delta\boldsymbol{u} \in \mathcal{U}_0, \\ &a(\boldsymbol{u}, \delta\boldsymbol{u}) := \int_\Omega \boldsymbol{\sigma} : \delta\boldsymbol{\varepsilon} \; d\boldsymbol{x}, \quad \ell(\delta\boldsymbol{u}) := \int_{\Gamma_t} \bar{\boldsymbol{t}} \cdot \delta\boldsymbol{u} \, dS, \end{aligned} \tag{10}$$

where $\mathcal{U}$ and $\mathcal{U}_0$ are the displacement trial and test spaces, respectively, δ is the first variation operator, and $\boldsymbol{\varepsilon}$ is the small strain tensor. The Cauchy stress tensor $\boldsymbol{\sigma}$ is related to $\boldsymbol{\varepsilon}$ through a linear elastic constitutive law: $\boldsymbol{\sigma} = \mathbb{C} : \boldsymbol{\varepsilon}$, where $\mathbb{C}$ is the fourth-order material moduli tensor.

3.2. Displacement approximation and discrete equations

The two-dimensional displacement approximation for crack modeling in the X-FEM is [1]:

$$\boldsymbol{u}_e^h(\boldsymbol{x}) = \sum_{i \in \mathbb{I}} N_i(\boldsymbol{x}) \boldsymbol{u}_i + \sum_{j \in \mathbb{J} \subseteq \mathbb{I}} N_j(\boldsymbol{x}) H(\boldsymbol{x}) \boldsymbol{a}_j + \sum_{t=1}^{2} \sum_{k \in \mathbb{K}_t \subseteq \mathbb{I}} N_k(\boldsymbol{x}) \sum_{\alpha=1}^{4} F_{\alpha t}(\boldsymbol{x}) \boldsymbol{b}_{k\alpha t}, \tag{11a}$$

where $N_i(\boldsymbol{x})$ are the standard finite element shape functions,

$$H(\boldsymbol{x}) = \begin{cases} 1 & \text{if } d(\boldsymbol{x}) \geq 0 \\ -1 & \text{if } d(\boldsymbol{x}) < 0 \end{cases} \tag{11b}$$

is a discontinuous (generalized Heaviside) function, where $d(\boldsymbol{x})$ is the signed distance to a crack, and

$$F_{\alpha t}(\boldsymbol{x}) := \sqrt{r} \left\{ \sin\frac{\theta}{2}, \; \cos\frac{\theta}{2}, \; \sin\frac{\theta}{2}\sin\theta, \; \cos\frac{\theta}{2}\sin\theta \right\} \tag{11c}$$

Prepared using nmeauth.cls
DOI: 10.1002/nme

are *near-tip* functions with r and θ defined for each crack tip t. In addition, $\boldsymbol{u}_i$, $\boldsymbol{a}_j$, and $\boldsymbol{b}_{k\alpha t}$ are degrees of freedom associated with standard finite element, Heaviside-enriched and near-tip enriched basis functions, respectively. The set $\mathbb{I}$ contains all nodes in element e, and the sets $\mathbb{J}$ and $\mathbb{K}_t$ $(t = 1, 2)$ include Heaviside-enriched and crack-tip-enriched nodes, respectively.

On using trial and test approximations of the form (11a) and following a standard Galerkin procedure, the discrete equations for the X-FEM are obtained: $\boldsymbol{K}\boldsymbol{d} = \boldsymbol{f}$, where the stiffness matrix $\boldsymbol{K}$ and the force vector $\boldsymbol{f}$ are computing using element-level assembly procedures. We use the indices u, a, and b to denote degrees of freedom associated with standard finite element basis functions, Heaviside-enriched basis function, and near-tip-enriched basis functions, respectively. The element stiffness matrix for the X-FEM assumes the form:

$$\boldsymbol{K}_e = \int_{\Omega_e} \begin{bmatrix} \boldsymbol{B}_u^T\boldsymbol{D}\boldsymbol{B}_u & \boldsymbol{B}_u^T\boldsymbol{D}\boldsymbol{B}_a & \boldsymbol{B}_u^T\boldsymbol{D}\boldsymbol{B}_b \\ \boldsymbol{B}_a^T\boldsymbol{D}\boldsymbol{B}_u & \boldsymbol{B}_a^T\boldsymbol{D}\boldsymbol{B}_a & \boldsymbol{B}_a^T\boldsymbol{D}\boldsymbol{B}_b \\ \boldsymbol{B}_b^T\boldsymbol{D}\boldsymbol{B}_u & \boldsymbol{B}_b^T\boldsymbol{D}\boldsymbol{B}_a & \boldsymbol{B}_b^T\boldsymbol{D}\boldsymbol{B}_b \end{bmatrix} dA = \int_{\Omega_e} \begin{bmatrix} \boldsymbol{K}_{uu} & \boldsymbol{K}_{ua} & \boldsymbol{K}_{ub} \\ \boldsymbol{K}_{au} & \boldsymbol{K}_{aa} & \boldsymbol{K}_{ab} \\ \boldsymbol{K}_{bu} & \boldsymbol{K}_{ba} & \boldsymbol{K}_{bb} \end{bmatrix} dA, \quad (12)$$

where $\boldsymbol{D}$ is the two-dimensional linear elastic constitutive matrix and the submatrix $\boldsymbol{K}_{uu}$ is the standard finite element stiffness matrix. The entries in the symmetric submatrix $\boldsymbol{K}_{ua}$ contain discontinuous functions, whereas the entries in the symmetric submatrices $\boldsymbol{K}_{ub}$, $\boldsymbol{K}_{ab}$ and $\boldsymbol{K}_{bb}$ consist of both weakly singular and discontinuous functions. The matrix $\boldsymbol{B}_i$ in (12) is:

$$\boldsymbol{B}_i = \begin{bmatrix} \boldsymbol{B}_i^1 & \boldsymbol{B}_i^2 & \dots & \boldsymbol{B}_i^{\mathrm{card}(\mathbb{L})} \end{bmatrix}.$$

For $i = u$, $\mathbb{L} = \mathbb{I}$ and

$$\boldsymbol{B}_u^\ell = \begin{bmatrix} N_{\ell,x}(\boldsymbol{x}) & 0 \\ 0 & N_{\ell,y}(\boldsymbol{x}) \\ N_{\ell,y}(\boldsymbol{x}) & N_{\ell,x}(\boldsymbol{x}) \end{bmatrix}.$$

For $i = a$, we have $\mathbb{L} = \mathbb{J}$ and $\boldsymbol{B}_a^\ell = H(\boldsymbol{x})\boldsymbol{B}_u^\ell$. For $i = b$, we have $\mathbb{L} = \mathbb{K}_t$ and

$$\boldsymbol{B}_b^\ell = \begin{bmatrix} \boldsymbol{B}_b^{\ell 1} & \boldsymbol{B}_b^{\ell 2} & \boldsymbol{B}_b^{\ell 3} & \boldsymbol{B}_b^{\ell 4} \end{bmatrix}.$$

Prepared using nmeauth.cls
DOI: 10.1002/nme

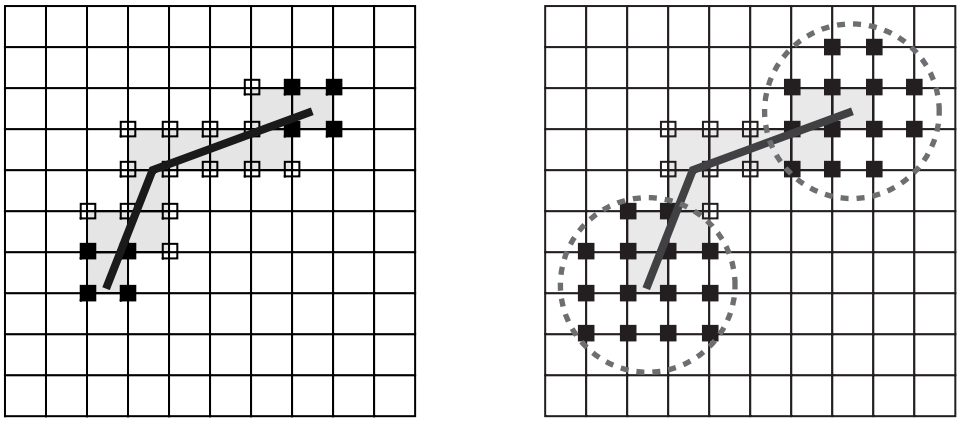

(a) (b)

Figure 3. Heaviside and near-tip enriched nodes. (a) Topological enrichment; and (b) Geometrical enrichment. The crack in shown as a thick line. Hollow squares indicate Heaviside-enriched nodes and filled squares indicate near-tip-enriched nodes. Elements that are cut by the crack are shaded grey. A grey, dotted circle is the geometrically enriched region: all nodes within this circle are enriched with the near-tip functions.

where

$$\boldsymbol{B}_b^{\ell\alpha} = \begin{bmatrix} \big(F_{\alpha t}(\boldsymbol{x})N_\ell(\boldsymbol{x})\big)_{,x} & 0 \\ 0 & \big(F_{\alpha t}(\boldsymbol{x})N_\ell(\boldsymbol{x})\big)_{,y} \\ \big(F_{\alpha t}(\boldsymbol{x})N_\ell(\boldsymbol{x})\big)_{,y} & \big(F_{\alpha t}(\boldsymbol{x})N_\ell(\boldsymbol{x})\big)_{,x} \end{bmatrix}.$$

The presence of enriched degrees-of-freedom within an element depends on the location of the element with respect to the cracks in the domain. Two strategies are adopted for near-tip enrichment: *topological* and *geometric* [11, 12]. In topological enrichment, only nodal finite element basis functions whose supports contain the crack-tip are enriched, whereas in geometric enrichment, all nodes that lie within a user-specified distance from the crack tip are enriched. Elements that are cut by a crack and whose nodes have not been assigned for near-tip enrichment are selected as Heaviside-enriched nodes. Figure 3 shows the selection of nodes for Heaviside and crack-tip enrichment.

3.3. Post-processing

Determining a material's susceptibility to fracture and fatigue crack growth requires extracting crack-tip characterizing parameters such as the J-integral and the mixed-mode stress intensity

Prepared using nmeauth.cls DOI: 10.1002/nme

factors. Computation of SIFs is facilitated through superimposing the field quantities of a known SIF solution (*auxiliary field*) on the field quantities of the (extended) finite element solution [21]. We denote the auxiliary field by superscript (2) and the extended finite element solution by superscript (1). On using the relation between the strain energy release rate and the stress intensity factors for the superimposed fields, the following equality is derived [21]:

$$I^{(1,2)} = \frac{2}{E'}\left[K_I^{(1)}K_I^{(2)} + K_{II}^{(1)}K_{II}^{(2)}\right], \tag{13}$$

where $I^{(1,2)}$ is the *interaction integral* or M-integral, for the crack tip of interest. In (13), $E' = E$ and $E' = E/(1-\nu^2)$ for plane stress and plane strain conditions, respectively. In domain form, the interaction integral is [22]:

$$I^{(1,2)} = \int_A \left[\sigma_{ij}^{(1)}u_{i,1}^{(2)} + \sigma_{ij}^{(2)}u_{i,1}^{(1)} - W^{(1,2)}\delta_{1j}\right] w_{,j}\, dA, \tag{14}$$

where $W^{(1,2)} = \sigma_{ij}^{(1)}\varepsilon_{ij}^{(2)} = \sigma_{ij}^{(2)}\varepsilon_{ij}^{(1)}$ is the interaction strain energy and $w \in C^0(A)$ is a weight function that is unity at the crack tip, vanishes on the boundary of A, and is otherwise arbitrary. In the computations, all elements that lie within a user-specified radius from the crack tip are used to define the domain A. To simplify implementation and reduce computations, $w(\boldsymbol{x})$ is chosen as a *plateau* function and is constructed through finite element interpolation by prescribing its nodal values: zero on nodes that lie on ∂A and unity at all other nodes. In an extended finite element implementation, the interaction integral is computed on elements that lie within A, and these contributions are summed to determine the integral in (14).

On choosing the auxiliary field corresponding to $K_I = 1$ and $K_{II} = 0$ (respectively, $K_I = 0$ and $K_{II} = 1$) allows K_I (respectively, K_{II}) to be extracted from an extended finite element solution in a straightforward manner. Let us refer to the resulting M-integral from this auxiliary field as $I^{(1,I)}$ (respectively, $I^{(1,II)}$). Performing this substitution in (13) yields

$$K_I = \frac{E'}{2}I^{(1,I)}, \quad K_{II} = \frac{E'}{2}I^{(1,II)}.$$

The mode I and mode II plane strain auxiliary fields are listed in Table I. Note that all functions are weakly singular and some that depend on $\sin(\theta/2)$ are also discontinuous along

Prepared using nmeauth.cls
DOI: 10.1002/nme

Table I. Mode I and mode II plane strain auxiliary displacement and stress fields.

Field	Mode I	Mode II
u_x	$\frac{K_I}{\mu}\sqrt{\frac{r}{2\pi}}\cos\frac{\theta}{2}\left[1-2\nu+\sin^2\frac{\theta}{2}\right]$	$\frac{K_{II}}{\mu}\sqrt{\frac{r}{2\pi}}\sin\frac{\theta}{2}\left[2-2\nu+\cos^2\frac{\theta}{2}\right]$
u_y	$\frac{K_I}{\mu}\sqrt{\frac{r}{2\pi}}\sin\frac{\theta}{2}\left[2-2\nu-\cos^2\frac{\theta}{2}\right]$	$\frac{K_{II}}{\mu}\sqrt{\frac{r}{2\pi}}\cos\frac{\theta}{2}\left[-1+2\nu+\sin^2\frac{\theta}{2}\right]$
σ_{xx}	$\frac{K_I}{\sqrt{2\pi r}}\cos\frac{\theta}{2}\left(1-\sin\frac{\theta}{2}\sin\frac{3\theta}{2}\right)$	$-\frac{K_{II}}{\sqrt{2\pi r}}\sin\frac{\theta}{2}\left(2+\cos\frac{\theta}{2}\cos\frac{3\theta}{2}\right)$
σ_{yy}	$\frac{K_I}{\sqrt{2\pi r}}\cos\frac{\theta}{2}\left(1+\sin\frac{\theta}{2}\sin\frac{3\theta}{2}\right)$	$\frac{K_{II}}{\sqrt{2\pi r}}\cos\frac{\theta}{2}\sin\frac{\theta}{2}\cos\frac{3\theta}{2}$
σ_{xy}	$\frac{K_I}{\sqrt{2\pi r}}\cos\frac{\theta}{2}\sin\frac{\theta}{2}\cos\frac{3\theta}{2}$	$\frac{K_{II}}{\sqrt{2\pi r}}\cos\frac{\theta}{2}\left(1-\sin\frac{\theta}{2}\sin\frac{3\theta}{2}\right)$

$\theta=\pm\pi$; therefore, the integrand in (14) has some terms that are both weakly singular and discontinuous.

3.4. Homogeneous functions in the X-FEM

We use the HNI method to compute the entries in the element stiffness matrix and for the M-integral calculations. To apply this method, the integrands must be homogeneous. In the element stiffness matrix given in (12), $\boldsymbol{D}$ is a constant matrix and therefore it has degree of homogeneity $q=0$. The near-tip functions $F_{\alpha t}(\boldsymbol{x})$ and the generalized Heaviside function $H(\boldsymbol{x})$ are homogeneous functions of degree $q=1/2$ and $q=0$, respectively. In addition, the partial derivatives of $F_{\alpha t}(\boldsymbol{x})$ are homogeneous functions of degree $q=-1/2$. Note that integration must be performed in the local crack tip coordinate system so that the functions remain homogeneous. The only remaining components of the integrand are the shape functions and their derivatives. These components must be either homogeneous or written as a linear combination of homogeneous functions. For the M-integral given in (14), the auxiliary field quantities (stress and displacement gradient) are homogeneous functions of degree $q=-1/2$. Similar to the element stiffness matrix, the homogeneity of $\boldsymbol{\sigma}^{(1)}$ and $\boldsymbol{\varepsilon}^{(1)}$ are dependent on the homogeneity of the finite element shape functions. The weight function w is defined using the shape functions, so it too is dependent on their homogeneity. In this paper, we use shape

Prepared using nmeauth.cls
DOI: 10.1002/nme

functions for the linear triangle and the bilinear rectangle. Homogeneous forms of these shape functions are presented in Appendix A.

4. INTEGRATION OF DISCONTINUOUS AND WEAKLY SINGULAR FUNCTIONS

Unlike many other methods that separately treat discontinuous and weakly singular integrands in the X-FEM, the implementation of the HNI method is essentially the same for integrating both types of functions. Overall, the procedure can be described in three steps:

1. decompose each element that is cut by a crack into conforming polygons;
2. develop an appropriate cubature rule on each polygon; and
3. apply (7) to perform numerical integration.

An overview of each step follows and an illustrative example of the process is presented in Section 4.4. If a crack intersects an element, the element is decomposed into polygonal regions. Two cases arise depending on the location of the crack relative to the element.

1. The crack completely cuts the element. Here, the element is decomposed into two polygons over which integration is performed. This case is illustrated in Figure 4.
2. The crack terminates inside an element. In this case, the crack is duplicated (opposite orientations) and the cracked-element is a nonconvex polygon (see Figure 5). The nonconvex polygon in Figure 5b has 7 edges.

In both the above cases, integration is required over simple polygons (convex or nonconvex), rendering the use of the HNI scheme to be a natural fit.

The cubature points and weights required for integration are dependent on the type of function being integrated. For a polynomial integrand (entries in $\boldsymbol{K}_{ua}$) up to degree q, an n-point Gauss quadrature rule on each boundary edge with $n \geq (q+1)/2$ suffices for exact integration. The exactness of the cubature rule is verified in Section 4.1. However, for nonpolynomial integrands that appear in $\boldsymbol{K}_{ub}$, $\boldsymbol{K}_{ab}$, $\boldsymbol{K}_{bb}$, and also in the M-integral, accurate integration requires additional considerations. For this case, we introduce an adaptive cubature scheme in Section 4.2. The adaptive HNI scheme is compared to the generalized Duffy transformation in Section 4.3.

Finally, we apply (7) over each element subdomain to compute the integral. For weakly singular functions, integration is performed in local crack tip coordinates such that the

Prepared using nmeauth.cls
DOI: 10.1002/nme

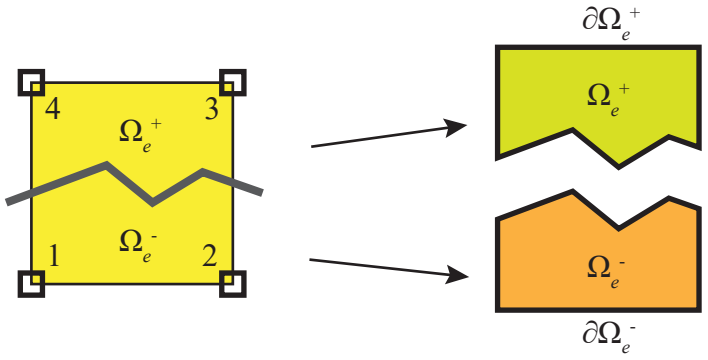

(a) (b)

Figure 4. (a) Heaviside-enriched element that is cut by a crack. (b) The HNI method is applied to the two resulting polygons, Ω_e^+ and Ω_e^-.

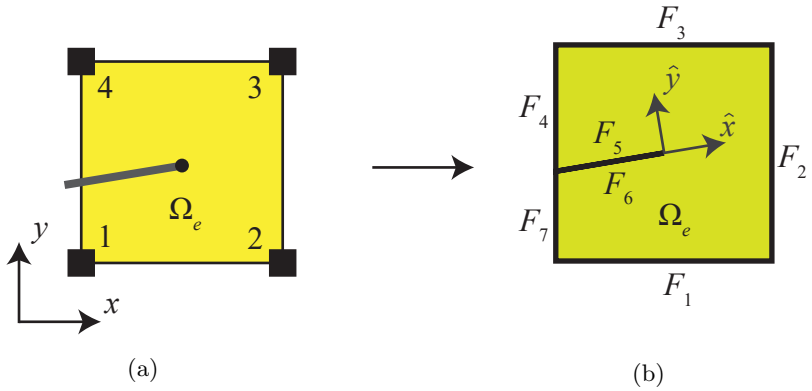

(a) (b)

Figure 5. (a) Element containing the crack tip has all nodes enriched with near-tip functions. (b) To apply the HNI method to this element, the cracked-element is viewed as a nonconvex polygon. The edges of the polygon are labeled as F_i.

integrand remains homogeneous. Since the mapping between crack tip and global coordinates is not homogeneous (see Appendix A), the homogeneous integrands change with the coordinate system. For polynomial integrands multiplied by the Heaviside function, integration can be done in global coordinates or in a local coordinate system.

4.1. Integration of a discontinuous function using the HNI method

We verify the accuracy of the HNI approach for integrating discontinuous functions. Consider the unit square domain $\Omega = [0, 1]^2$, which is fully cut by a (piecewise) affine discontinuity Γ_c.

Prepared using nmeauth.cls
DOI: 10.1002/nme

Let $u(\boldsymbol{x}) : \Omega \to \mathbb{R}$ be a scalar-valued function that is bilinear and discontinuous across Γ_c:

$$u(\boldsymbol{x}) = (1 + x + y + xy)H(\boldsymbol{x}), \tag{15}$$

where $H(\boldsymbol{x})$ is the generalized Heaviside function. We discretize Ω using rectangular finite elements and write the extended finite element approximation for $u(\boldsymbol{x})$ within an element as:

$$u_e^h(\boldsymbol{x}) = \sum_{i \in \mathbb{I}} N_i(\boldsymbol{x}) u_i + \sum_{j \in \mathbb{J} \subset \mathbb{I}} H(\boldsymbol{x}) N_j(\boldsymbol{x}) a_j.$$

The approximation $u_e^h(\boldsymbol{x})$ is the restriction of the global approximation, $u^h(\boldsymbol{x})$, to element e. If $\mathcal{U}_h$ is the extended finite element space, then we observe that $u \in \mathcal{U}_h$, and hence the best approximation in $\mathcal{U}_h$ should exactly reproduce $u(\boldsymbol{x})$. Therefore, $a_j = u(\boldsymbol{x}_j)$ and $u_j = 0$ for $j \in \mathbb{J}$.

The best approximation to $u(\boldsymbol{x})$ is obtained by determining the L_2 projection of $u(\boldsymbol{x})$ on $\mathcal{U}_h$. The coefficients $\boldsymbol{d} := \{\boldsymbol{u}, \boldsymbol{a}\}$ are obtained as the solution of the linear system: $\boldsymbol{M}\boldsymbol{d} = \boldsymbol{f}$, where the mass matrix $\boldsymbol{M}$ and force vector $\boldsymbol{f}$ are formed by element-level assembly procedures. The element mass matrix and the element force are:

$$(\boldsymbol{M}_e)_{ij} = \int_{\Omega_e} \tilde{N}_i(\boldsymbol{x}) \tilde{N}_j(\boldsymbol{x}) \, dA, \quad (\boldsymbol{f}_e)_i = \int_{\Omega_e} \tilde{N}_i(\boldsymbol{x}) u(\boldsymbol{x}) \, dA,$$

where $\tilde{N}_i(\boldsymbol{x}) = N_i(\boldsymbol{x})$ for standard degrees-of-freedom and $\tilde{N}_i(\boldsymbol{x}) = H(\boldsymbol{x}) N_i(\boldsymbol{x})$ for Heaviside-enriched degrees-of-freedom. The evaluation of $\boldsymbol{M}_e$ and $\boldsymbol{f}_e$ requires integrating discontinuous polynomials; this exercise can be viewed as a *patch test* for discontinuous approximations.

For the test, we use a 3×3 patch of elements. Two discontinuities are considered: an affine crack and a kinked-crack that are shown in Figures 6a and 6b, respectively. For discontinuous integrands, the HNI method is used with a three-point quadrature rule on each of the bounding line segments of the element subdomains. For integrating smooth polynomials within the element, 2×2 tensor-product Gauss rule is used. The function $u(\boldsymbol{x})$ for the kinked discontinuity is shown in Figure 6c, and the error $|u - u^h|$ is presented in Figure 6d. The approximation $u^h(\boldsymbol{x})$ matches $u(\boldsymbol{x})$ to a precision of $\mathcal{O}(10^{-13})$ or better for both the affine and kinked discontinuities. As Figure 6d illustrates, the error in the approximation increases in enriched elements that are farther away from the origin. This is a consequence of integrating in global coordinate system

Prepared using nmeauth.cls
DOI: 10.1002/nme

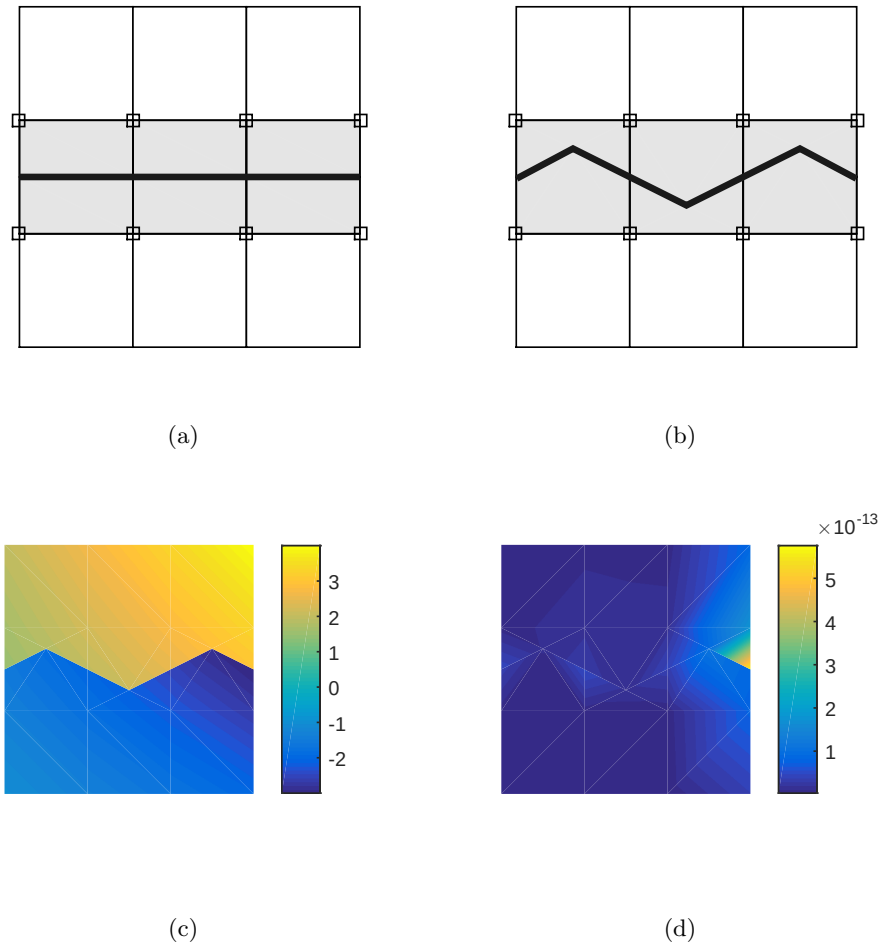

Figure 6. L_2 projection of a discontinuous bilinear function on an extended finite element approximation (3×3 finite element mesh). (a) Affine crack; and (b) Kinked crack. For the kinked discontinuity in (b), $u(\boldsymbol{x})$ is plotted in (c) and the error $|u(\boldsymbol{x}) - u^h(\boldsymbol{x})|$ is shown in (d).

rather than a local element coordinate system. Using the HNI method in global coordinates results in contributions that are close in magnitude but opposite in sign, which leads to loss of a few significant digits. This can be remedied by performing the integration in a local element coordinate system. The Heaviside degrees-of-freedom a_j match $u(\boldsymbol{x}_j)$ (13 or more digits of precision) and u_j ($j \in \mathbb{J}$) is zero to 13 digits. Based on these findings, we affirm that the HNI approach provides accurate and efficient numerical integration for discontinuous polynomials.

4.2. Adaptive HNI scheme

Homogeneous numerical integration converts a domain integral over a polygon to an integral over the bounding line segments of a polygon. If the singular point is within the domain of integration, then this leaves only the computation of the integral of a smooth function over

Prepared using nmeauth.cls
DOI: 10.1002/nme

Algorithm 1 Adaptive HNI scheme.

Require: $\bar{f}(\boldsymbol{x}), n_1, n_2, coord, conn, m, tol$
  x_1 and $w_1 \leftarrow n_1$-point Gauss rule ▷ $x_\alpha = (n_\alpha \times 1)$ array of Gauss points
  x_2 and $w_2 \leftarrow n_2$-point Gauss rule ▷ $w_\alpha = (n_\alpha \times 1)$ array of Gauss weights
  $\boldsymbol{x}_f \leftarrow [\,]$, $w_f \leftarrow [\,]$ ▷ subscript f denotes final
  for $i = 1$ to m **do**
    $\beta_i \leftarrow b_i/\|\boldsymbol{a}_i\|$ for the current edge of the polygon
    $\ell_i \leftarrow$ length of the current edge of the polygon
    if $|\beta_i| > tol$ **then**
      $\boldsymbol{\xi}_{int} \leftarrow [-1, 1]$ ▷ $(n_{int} \times 2)$ array of integration intervals
      $n_{int} \leftarrow 1$ ▷ number of integration intervals
      $c_{int} \leftarrow 1$ ▷ current integration interval
      while $c_{int} \leq n_{int}$ **do**
        $w_{int} \leftarrow \boldsymbol{\xi}_{int}(c_{int}, 2) - \boldsymbol{\xi}_{int}(c_{int}, 1)$ ▷ width of current interval
        for $j = 1$ to 2 **do**
          $\boldsymbol{xloc}_j \leftarrow x_j$ mapped to current interval on current edge of the polygon
          $wloc_j \leftarrow (w_{int} \times \ell_i/4) \times w_j$ ▷ local Gauss weights
          $I_j \leftarrow 0$
          for $k = 1$ to n_j **do**
            $I_j \leftarrow I_j + \bar{f}(\boldsymbol{xloc}_j(k, :)) \times wloc_j(k)$
          end for
        end for
        if $|(I_1 - I_2)/I_2| < (tol \times w_{int}/2)$ **then**
          $\boldsymbol{x}_f \leftarrow [\boldsymbol{x}_f;\, \boldsymbol{xloc}_1]$
          $w_f \leftarrow [w_f;\, \beta_i \times wloc_1]$
          $c_{int} \leftarrow c_{int} + 1$
        else
          Bisect $\boldsymbol{\xi}_{int}(c_{int}, :)$
          $n_{int} \leftarrow n_{int} + 1$
        end if
      end while
    end if
  end for
  return $\boldsymbol{x}_f$, w_f

the boundary of the polygon. Further, if the singular point lies on the boundary and coincides with one of the bounding line segments, then no contribution arises from this line integral. This is established by noting that for weakly singular homogeneous functions, singularities appear at the origin. For lines that pass through the origin, we have $b/\|\boldsymbol{a}\| = 0$, and therefore the line segment has no contribution to the integral. These two observations reveal why the HNI approach is effective for weakly singular functions. However, bounding line segments may still lie very close to the singular point, resulting in a *nearly singular* integrand.

Polynomial approximation of a nearly singular integrand is poor, and hence many quadrature points are needed to meet a desired accuracy. To optimize the distribution of quadrature points required on each line segment, we adopt an adaptive quadrature scheme.

Prepared using nmeauth.cls
DOI: 10.1002/nme

This scheme provides an optimized, custom cubature rule for each element and it allows for integrals to be calculated to a user-specified precision through an *a posteriori* estimation of the error.

In the simplified pseudocode for the adaptive scheme presented in Algorithm 1, Matlab notation is adopted (brackets, colon, and semi-colon) to define matrices and vectors and to access rows or columns of a matrix. Indexing for matrices begins at 1. The algorithm requires

1. $\bar{f}(\boldsymbol{x})$: linear combination of homogeneous functions that is to be integrated.
2. $[n_1, n_2]$: the number of quadrature points for the Gauss rules ($n_2 > n_1$).
3. *coord*: coordinates of the vertices of the polygon.
4. *conn*: connectivity of the vertices that form the polygon.
5. m : number of edges of the polygon.
6. *tol* : convergence tolerance.

In the adaptive scheme, the integral of $\bar{f}(\boldsymbol{x})$ within a subinterval of the domain of integration is estimated using n_1- and n_2-point Gauss rules. Their absolute difference provides an estimate of the error, which is used to assess convergence within the subinterval. The algorithm is designed to loop over each bounding line segment defined by *conn*. On each line segment, an n_1-point Gauss rule is tested to see if sufficiently accurate integration is realized. If not, the line segment is bisected and an n_1-point rule is tested on the two resulting subintervals of the line segment. The bisection process continues until an n_1-point Gauss rule provides sufficient accuracy over each subinterval of the line segment.

Empirically, for the weakly singular integrals that appear in the X-FEM, $n_1 = 5$, $n_2 = 8$, $\bar{f}(\boldsymbol{x}) = (1/r + \sqrt{1/r})$, and $tol = 10^{-8}$ strikes a sound balance between accuracy of the rule and the total number of quadrature points that are needed. With these parameters, the adaptive cubature rule has an average relative error of $\mathcal{O}(10^{-8})$ for integrating the entries in $\boldsymbol{K}_e$. As Figure 7 reveals, the accuracy varies with spatial location and rotation of the element with respect to the crack tip. Figure 7 also shows that the accuracy is improved at a linear rate by decreasing *tol*. Additionally, note that $\bar{f}(\boldsymbol{x})$ is not a homogeneous function. This is permitted in Algorithm 1 since $\bar{f}(\boldsymbol{x})$ is only used to assess if and when the cubature rule converges. Finally, contrary to expectations, we find that introducing trigonometric functions into $\bar{f}(\boldsymbol{x})$ does not lead to improvements in the convergence rate of the integration scheme.

The distribution of cubature points on the bounding line segments of an element as a function of the location of the crack is illustrated in Figure 8. As expected, when the crack tip

Prepared using nmeauth.cls
DOI: 10.1002/nme

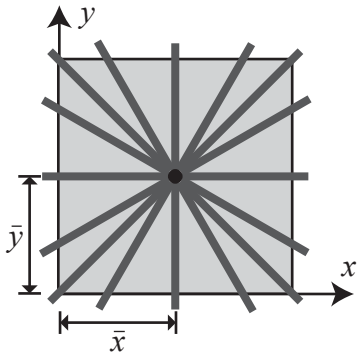

(a)

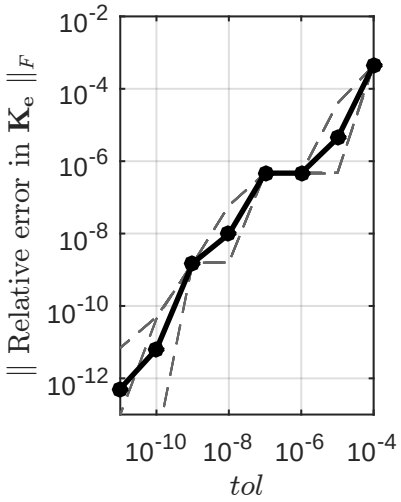

(b) $\bar{x} = \bar{y} = 1/2$

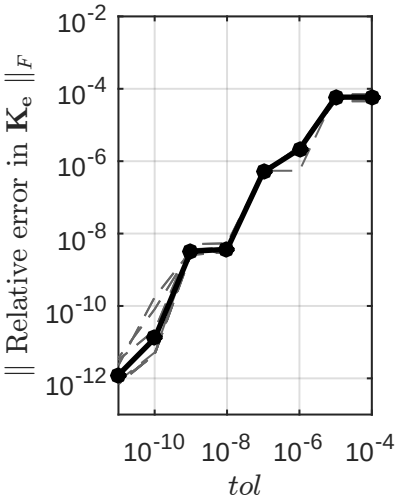

(c) $\bar{x} = 1/2, \bar{y} = 1/500$

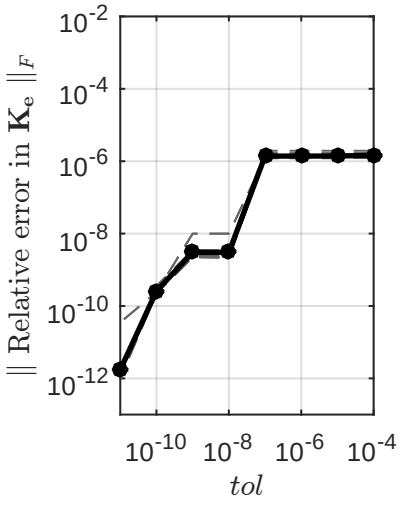

(d) $\bar{x} = \bar{y} = 1/500$

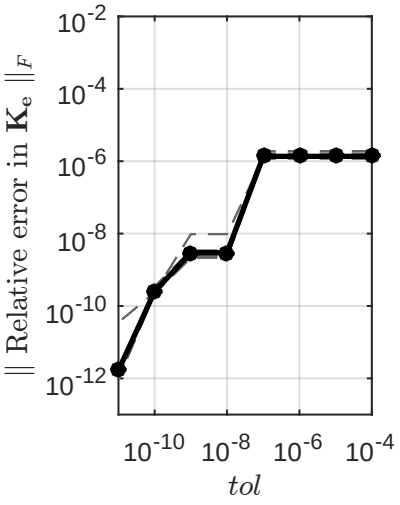

(e) $\bar{x} = \bar{y} = 0$

Figure 7. Frobenius norm of relative error in $\boldsymbol{K}_e$ as a function of *tol* using the adaptive quadrature scheme. (a) Crack configurations that cut the unit square. The crack-tip is located at $(\bar{x}, \bar{y})$. Four different crack-tip locations are tested, which appear in (b), (c), (d) and (e). At each crack-tip, the procedure is repeated for 16 cracks inclined at different angles, which are shown in (a). Results for each inclined crack are plotted with dashed lines in (b)–(e) and the solid line gives the log-average of all cracks.

Prepared using nmeauth.cls
DOI: 10.1002/nme

is close to the edge of the element, more quadrature points are needed on nearby line segments. This is also true for the results presented in Figure 7. The variation of the error as function of *tol* is similar in Figures 7d and 7e; however, many more cubature points are needed for a particular value of *tol* in Figure 7d vis-à-vis that in Figure 7e.

4.3. Comparison of the adaptive HNI scheme to the generalized Duffy transformation

We compare the accuracy of the generalized Duffy transformation [8], a singularity-canceling method effective with the X-FEM, to the adaptive HNI scheme for computing the weakly singular integrals that appear in $\boldsymbol{K}_e$. In particular, we examine the case where the crack tip approaches the edge of an element and compare the two methods of integration in terms of both solution accuracy and number of quadrature points. In addition to considering the element Ω_1, which contains the crack tip, the adjacent element Ω_2 is also included in our analyses. Since generalized Duffy cannot be used in elements adjacent to the crack tip, we use higher-order Gauss quadrature in Ω_2.

The configuration of elements used in the study is depicted in Figure 9. Geometric enrichment is used so that all nodes in both elements contain near-tip enrichment. In Figure 9, the distance from the crack tip to the common edge between the two elements is denoted by Δx. Four different values of Δx are tested: $\Delta x = 0.25$, 0.1, 0.01, and 0.001. To quantify the accuracy of each integration method, we compute the Frobenius norm of the relative error in $\boldsymbol{K}_e$. The norm of the relative error in $\boldsymbol{K}_e$ versus the number of quadrature points for these four values of Δx is shown in Figure 10. Convergence is plotted for elements Ω_1 and Ω_2 using HNI and either generalized Duffy or Gauss cubature for integration. For the HNI scheme, $tol = 10^{-8}$ is used. Numerical integration using the generalized Duffy map is performed with the parameter $\beta = 2$ to accurately integrate weakly singular functions of the form r^{-1} and $r^{-1/2}$ in the X-FEM [8].

For the four crack locations shown in Figure 10, the adaptive HNI scheme almost always provides more accurate integration using fewer cubature points. The advantage of HNI grows in relation to the other methods as the crack shifts closer to the edge common to Ω_1 and Ω_2. In the most challenging case ($\Delta x = 0.001$), HNI produces an error of less than $\mathcal{O}(10^{-10})$ with fewer than 500 cubature points in both Ω_1 and Ω_2. The relative error could not be reduced below $\mathcal{O}(10^{-4})$ with generalized Duffy in Ω_1 or using Gauss cubature in Ω_2, even with a ten-fold increase in the number of cubature points.

Prepared using nmeauth.cls
DOI: 10.1002/nme

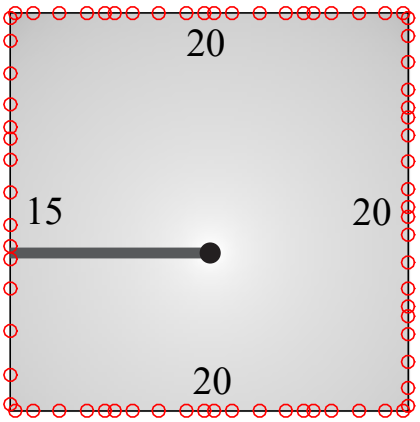

(a)

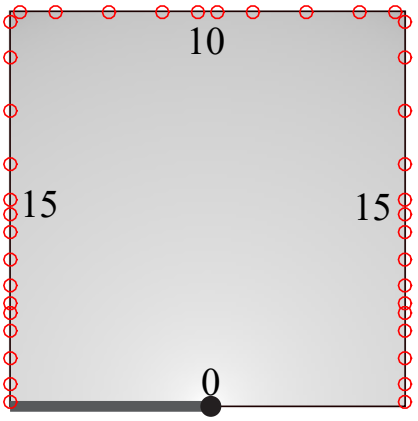

(b)

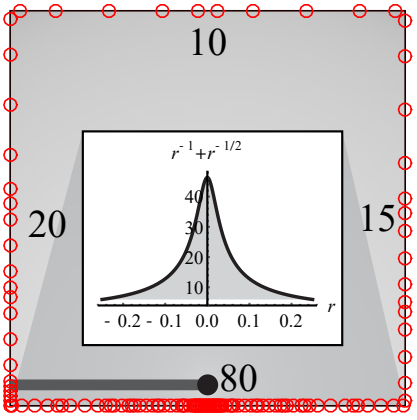

(c)

Figure 8. Distribution of cubature points for three different crack-tip locations in a unit square. Cubature points are marked by circles and the crack is a thick line. Convergence tolerance $tol = 10^{-8}$. In (a), the crack tip is located at $(1/2, 2/5)$ and 75 cubature points are needed for convergence. In (b), the crack-tip is located at $(1/2, 0)$ and only 40 cubature points are needed. In (c), the crack-tip is located at $(1/2, 1/20)$ resulting in a nearly singular integrand on the line segment occupying $0 < x < 1$, $y = 0$. The shape of the integrand is also plotted in (c). A total of 125 cubature points are needed.

Prepared using nmeauth.cls
DOI: 10.1002/nme

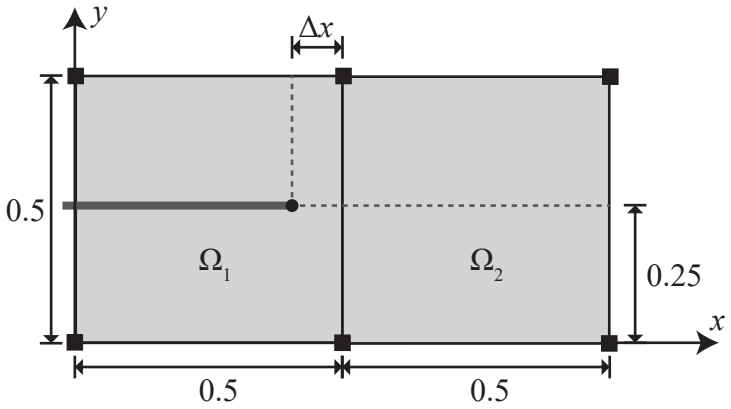

Figure 9. Test to compare the HNI approach to integration using generalized Duffy in Ω_1 and higher-order Gauss cubature in Ω_2. The crack (thick line) and crack tip (filled circle) reside in Ω_1.

Another point worth mentioning is that the parameter *tol*, which is a user-specified tolerance in the adaptive HNI scheme, provides a measure of reliability and accuracy in computing weakly singular integrals. No such control on the error is available for schemes based on generalized Duffy and Gauss cubature. Although forming the adaptive quadrature rule increases computational costs, the overall time spent in computing integrals in the adaptive HNI method is significantly less than generalized Duffy in our implementation of these schemes. This does not include the time to partition the enriched elements, which is required with generalized Duffy but not with homogeneous numerical integration.

4.4. Implementation of the HNI method

We describe the key steps to implement HNI for integrating discontinuous and weakly singular functions in the X-FEM. As an example, a rectangular element with both Heaviside and near-tip enriched nodes is considered (Figure 11). For elements with only Heaviside or only near-tip enriched nodes, the implementation of HNI is a simplified version of this case. For the linear triangle, the implementation is very similar to that of the bilinear rectangle.

To form the element stiffness matrix (12) using the X-FEM, we need to integrate functions that are:

1. continuous[†]: $\boldsymbol{K}_{uu}$ and $\boldsymbol{K}_{aa}$,
2. discontinuous: $\boldsymbol{K}_{ua} = \boldsymbol{K}_{au}^T$, and

[†]From (11b), since $H^2 = 1$, $\boldsymbol{K}_{aa}$ is continuous.

Prepared using nmeauth.cls
DOI: 10.1002/nme

3. weakly singular: $\boldsymbol{K}_{ub} = \boldsymbol{K}_{bu}^T$, $\boldsymbol{K}_{ab} = \boldsymbol{K}_{ba}^T$, and $\boldsymbol{K}_{bb}$.

The HNI method is well-suited for these functions. First, the orientation of the crack is used to decompose the element into two rectangular subdomains (see Figure 11). For weakly singular

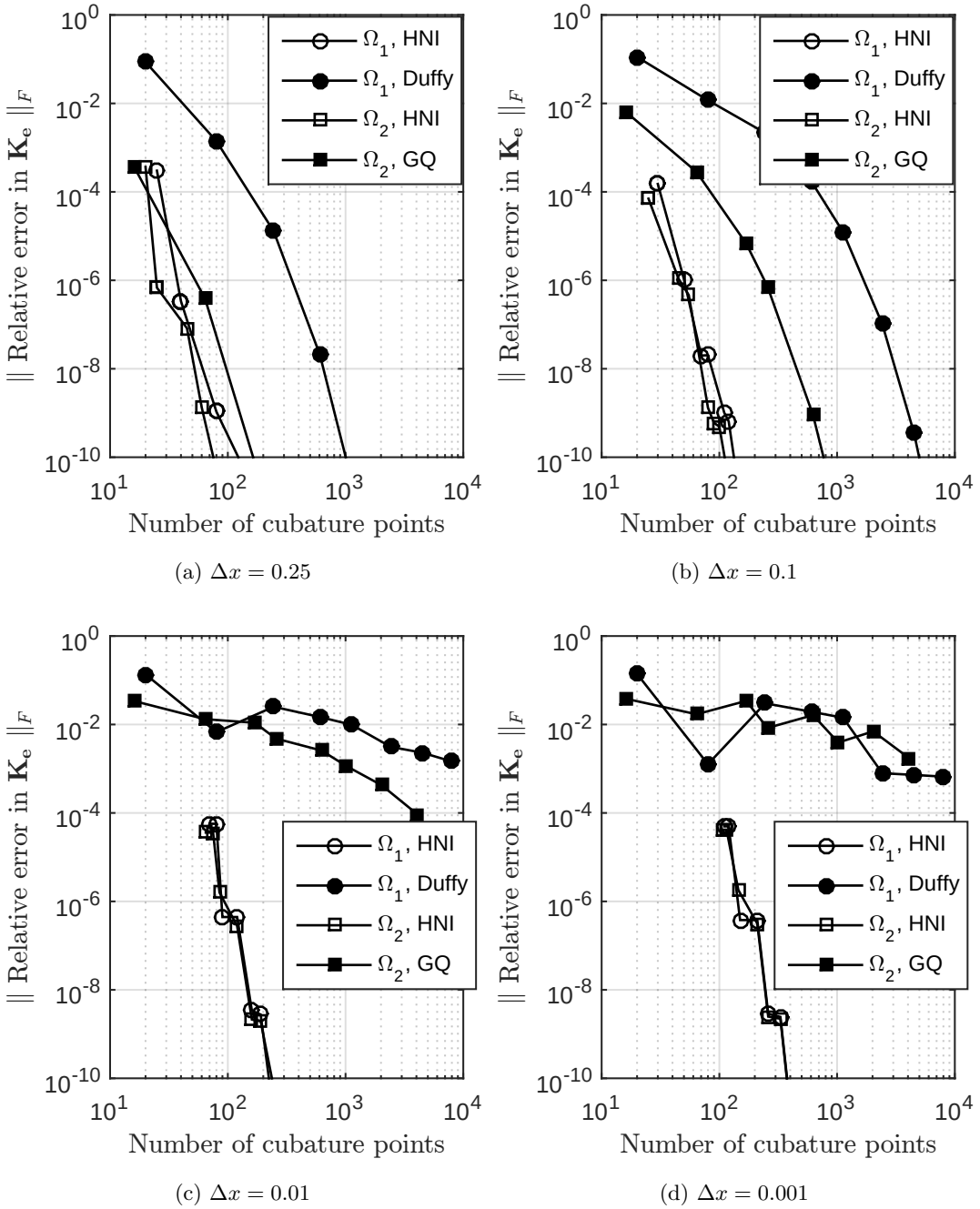

(a) $\Delta x = 0.25$ (b) $\Delta x = 0.1$

(c) $\Delta x = 0.01$ (d) $\Delta x = 0.001$

Figure 10. Relative error of the element stiffness matrix versus the number of cubature points for the HNI method and the generalized Duffy transformation/higher-order Gauss cubature. Four crack tip locations are considered: (a) center of Ω_1 ($\Delta x = 0.25$); (b) close ($\Delta x = 0.1$) to the edge that is common to Ω_1 and Ω_2; (c) $\Delta x = 0.01$; and (d) $\Delta x = 0.001$. Ω_1, Ω_2, and Δx are defined in Figure 9.

Prepared using nmeauth.cls
DOI: 10.1002/nme

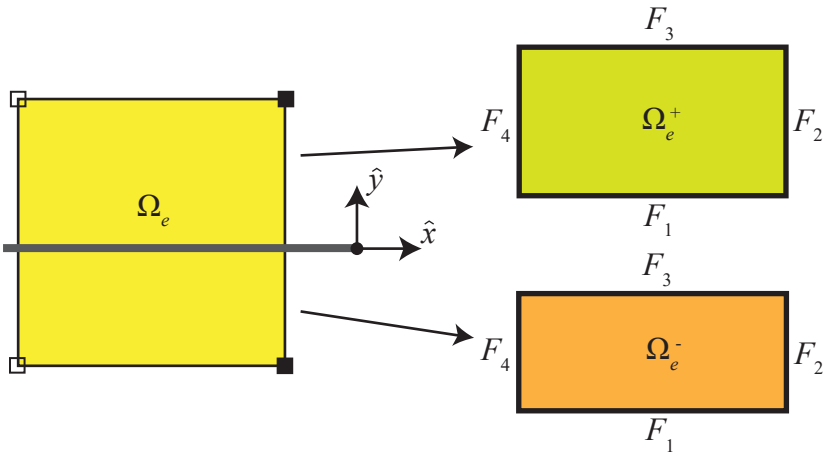

Figure 11. Element that is fully cut by a crack (left). Decomposition of the element into two polygons, which are used in the HNI method (right).

integrands that are homogeneous, we integrate in local crack tip coordinates. Even though continuous and discontinuous functions can be integrated in global coordinates, we choose to integrate these functions in local crack tip coordinates to simplify the implementation. For an element that does not have a crack tip associated with it (for example, an element with only Heaviside enrichment), integration can be performed in global coordinates or in a local element coordinate system.

A cubature rule for each of the subdomains is formed using the adaptive quadrature scheme introduced in Section 4.2. This cubature rule is designed to integrate the weakly singular functions in the element stiffness matrix, but it contains sufficient number of cubature points to accurately integrate the continuous and discontinuous functions as well. Though the cubature rule is not optimal for polynomials, a single cubature rule that is valid for all stiffness matrix entries reduces code-complexity and has minimal effect on computer-runtime. For an element stiffness matrix with discontinuous integrands but without weakly singular integrands, a two-point cubature rule on each bounding line segment suffices. For an element with only finite element degrees of freedom, 2×2 tensor-product Gauss cubature is used.

Once a cubature rule is on-hand, we use it in (7) to integrate element stiffness matrix entries. Since (7) requires the integrand to be separated into its homogeneous components, we must first homogenize each integrand. First, for the discontinuous integrand $\boldsymbol{K}_{ua} = \boldsymbol{B}_u^T \boldsymbol{D} \boldsymbol{B}_a$, the constitutive relation $\boldsymbol{D}$ is constant and is therefore homogeneous with $q = 0$, or for

Prepared using nmeauth.cls
DOI: 10.1002/nme

brevity $\boldsymbol{D}^{[0]}$[‡]. For the rectangular element, the shape function derivatives are affine functions (Table VII). As a result, the $\boldsymbol{B}_u$ and $\boldsymbol{B}_a$ matrices can be written as a linear combination of homogeneous matrices, or $\boldsymbol{B}_i = \boldsymbol{B}_i^{[0]} + \boldsymbol{B}_i^{[1]}$ for $i = u, a$. Overall, the integrand can be written as

$$\boldsymbol{K}_{ua} = \left(\boldsymbol{B}_u^{[0]} + \boldsymbol{B}_u^{[1]}\right)^T \boldsymbol{D}^{[0]} \left(\boldsymbol{B}_a^{[0]} + \boldsymbol{B}_a^{[1]}\right),$$

which allows $\boldsymbol{K}_{ua}$ to be decomposed into homogeneous components:

$$\boldsymbol{K}_{ua} = \boldsymbol{K}_{ua}^{[0]} + \boldsymbol{K}_{ua}^{[1]} + \boldsymbol{K}_{ua}^{[2]}.$$

On applying (7) to the homogeneous entries in $\boldsymbol{K}_{ua}$, with $H(\boldsymbol{x}) = 1$ in Ω_e^+ and $H(\boldsymbol{x}) = -1$ in Ω_e^-, we have

$$\begin{aligned}\int_{\Omega_e} \boldsymbol{K}_{ua}\, dA = &\sum_{k=1}^{nq^+} \tilde{w}_k \left(\frac{\boldsymbol{K}_{ua}^{[0]}(\boldsymbol{x}_k)}{2} + \frac{\boldsymbol{K}_{ua}^{[1]}(\boldsymbol{x}_k)}{3} + \frac{\boldsymbol{K}_{ua}^{[2]}(\boldsymbol{x}_k)}{4} \right) - \\ &\sum_{k=1}^{nq^-} \tilde{w}_k \left(\frac{\boldsymbol{K}_{ua}^{[0]}(\boldsymbol{x}_k)}{2} + \frac{\boldsymbol{K}_{ua}^{[1]}(\boldsymbol{x}_k)}{3} + \frac{\boldsymbol{K}_{ua}^{[2]}(\boldsymbol{x}_k)}{4} \right),\end{aligned}$$

where nq^+ is the number of cubature points in Ω_e^+ and nq^- is the number of cubature points in Ω_e^-.

The entries in $\boldsymbol{K}_{uu}$ and $\boldsymbol{K}_{aa}$ are continuous over the element, and can therefore be integrated using a tensor-product Gauss rule. However, since HNI is already used to compute discontinuous integrands in this element, $\boldsymbol{K}_{uu}$ and $\boldsymbol{K}_{aa}$ can also be integrated with minimal additional computations. As with $\boldsymbol{K}_{ua}$, a homogeneous decomposition of $\boldsymbol{K}_{uu}$ and $\boldsymbol{K}_{aa}$ results in three homogeneous matrices of degree $q = 0$, 1, and 2. Integration can be performed using (7) with the same cubature rule used for discontinuous and singular functions.

[‡]In this section, we denote the degree of homogeneity of a function with the superscript $[q]$.

Prepared using nmeauth.cls
DOI: 10.1002/nme

For the weakly singular functions, we can perform a similar homogeneous decomposition of the element stiffness matrix integrands, leaving

$$\begin{aligned}\boldsymbol{K}_{ub} &= \boldsymbol{K}_{ub}^{[-1/2]} + \boldsymbol{K}_{ub}^{[1/2]} + \boldsymbol{K}_{ub}^{[3/2]} + \boldsymbol{K}_{ub}^{[5/2]},\\ \boldsymbol{K}_{ab} &= \boldsymbol{K}_{ab}^{[-1/2]} + \boldsymbol{K}_{ab}^{[1/2]} + \boldsymbol{K}_{ab}^{[3/2]} + \boldsymbol{K}_{ab}^{[5/2]},\\ \boldsymbol{K}_{bb} &= \boldsymbol{K}_{bb}^{[-1]} + \boldsymbol{K}_{bb}^{[0]} + \boldsymbol{K}_{bb}^{[1]} + \boldsymbol{K}_{bb}^{[2]} + \boldsymbol{K}_{bb}^{[3]}.\end{aligned}$$

These functions can be integrated similarly to $\boldsymbol{K}_{ua}$ using (7). Since the cubature rule is shared among the three types of integrands, integration of all functions in the element stiffness matrix can be performed using a single loop over the cubature points.

In addition to computing stiffness matrix entries with HNI, we also apply the method to compute the M-integral. The expression for the M-integral is given in (14). For the element that is cut by a crack (Figure 11), the strain components are: $\boldsymbol{\varepsilon} = \boldsymbol{B}_u\boldsymbol{u} + \boldsymbol{B}_a\boldsymbol{a} + \boldsymbol{B}_b\boldsymbol{b}$. With homogeneous $\boldsymbol{B}$ matrices for the bilinear rectangle, the homogenized strain is:

$$\boldsymbol{\varepsilon} = \boldsymbol{\varepsilon}^{[-1/2]} + \boldsymbol{\varepsilon}^{[0]} + \boldsymbol{\varepsilon}^{[1/2]} + \boldsymbol{\varepsilon}^{[1]} + \boldsymbol{\varepsilon}^{[3/2]}.$$

Since stress components also have the same degree of homogeneity as strain components, we have

$$\boldsymbol{\sigma} = \boldsymbol{\sigma}^{[-1/2]} + \boldsymbol{\sigma}^{[0]} + \boldsymbol{\sigma}^{[1/2]} + \boldsymbol{\sigma}^{[1]} + \boldsymbol{\sigma}^{[3/2]}.$$

The auxiliary fields given in Table I are homogeneous of degree $q = -1/2$ and the weight function can be homogenized to produce $w_{,j} = w_{,j}^{[0]} + w_{,j}^{[1]}$. These components of the M-integral are combined to homogenize its integrand, resulting in homogeneous terms of degree $q = -1$, $-1/2$, 0, $1/2$, 1, $3/2$, and 2. For elements without near-tip enrichment, the number of homogeneous terms reduces to three, with degrees of $q = -1/2$, $1/2$, and $3/2$. The integrals of these functions are computed using (7) with an adaptive cubature rule. Note the field quantities in the M-integral are with respect to the local crack tip coordinate system. Since the rotation matrix used to transform field quantities is homogeneous of degree $q = 0$, rotation does not affect the homogeneity of the integrands.

Prepared using nmeauth.cls
DOI: 10.1002/nme

5. NUMERICAL EXAMPLES

In this section, we present three problems in elastic fracture to demonstrate the capabilities of the HNI scheme in the X-FEM to accurately integrate discontinuous and weakly singular functions. The three problems are: a plate with an edge-crack, a plate with an embedded inclined crack, and a plate with a piecewise affine embedded crack. Plane strain conditions are assumed with isotropic linear elastic material constants of $E = 10^5$ and $\nu = 0.3$. The X-FEM capabilities with HNI are developed within a code written in MATLAB$^{\text{TM}}$ Version R2015b. Where appropriate, results are compared to explicit flaw analyses done in Abaqus$^{\text{TM}}$ 6.13-1 [18] with refined, focused crack tip meshes.

5.1. Edge-cracked plate

Consider a square plate with an edge-crack. The plate occupies the domain $\Omega = [0, 5]^2$. The crack is a line segment that starts at $(0, 2.5)$ and terminates at the center of the plate. The crack is represented as a line segment and its vertices are stored in the matrix

$$\boldsymbol{C} = \begin{bmatrix} 0 & 2.5 \\ 2.5 & 2.5 \end{bmatrix}. \tag{16}$$

On the boundary of the plate, pure mode I displacement fields are applied as essential boundary conditions and therefore the mode I displacement fields are the exact solution. We test convergence of the extended finite element solution to the exact solution on triangular and rectangular meshes with both topological and geometric enrichment. A similar convergence study is conducted in Mousavi and Sukumar [8].

Typical triangular and rectangular meshes with topological enrichment are presented in Figure 12. With rectangular elements, the crack faces coincide with element boundaries, so element-partitioning is not needed. As a result, the HNI approach is not invoked for elements with Heaviside-enriched nodes. Near-tip enriched elements, on the other hand, do require use of benefit from accurate integration provided by the HNI method. Note that the crack tip lies on the boundary of four elements, causing full near-tip enrichment in all four elements. For unstructured triangular meshes, HNI is used on both Heaviside enriched and near-tip enriched elements. A double node is placed at $(0, 2.5)$, so that essential boundary conditions can be easily applied at this location.

Prepared using nmeauth.cls
DOI: 10.1002/nme

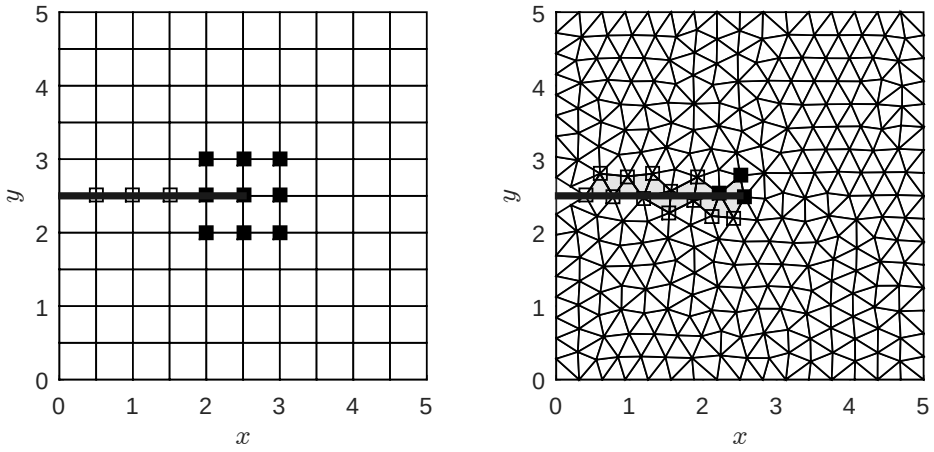

Figure 12. The edge-cracked domain meshed with (a) rectangular and (b) triangular elements. In (a) and (b), the crack is shown as a thick line, Heaviside-enriched nodes are marked with hollow squares, and near-tip-enriched nodes are marked with filled squares.

We define the relative energy seminorm of the error as:

$$E_{rel} := \left[\frac{a(\boldsymbol{u}-\boldsymbol{u}^h, \boldsymbol{u}-\boldsymbol{u}^h)}{a(\boldsymbol{u},\boldsymbol{u})}\right]^{1/2} = \left[\frac{\int_\Omega \left(\boldsymbol{\varepsilon}-\boldsymbol{\varepsilon}^h\right)^T \boldsymbol{D}\left(\boldsymbol{\varepsilon}-\boldsymbol{\varepsilon}^h\right) d\boldsymbol{x}}{\int_\Omega \boldsymbol{\varepsilon}^T \boldsymbol{D}\boldsymbol{\varepsilon}\, d\boldsymbol{x}}\right]^{1/2},$$

where $a(\cdot,\cdot)$ is the bilinear form defined in (10), and $\boldsymbol{\varepsilon}$ and $\boldsymbol{\varepsilon}^h$ are the exact strains and the strains from the extended finite element solution, respectively. The relative energy seminorm of the error is plotted versus h (mesh size) in Figure 13. Five different mesh densities, ranging from $h = 0.5$ to $h = 0.03125$ are chosen. Using HNI with a relatively low tolerance in the adaptive cubature rule ($tol = 10^{-4}$) provides the expected rates of convergence of 1/2 for topological enrichment and 1 for geometric enrichment on both triangular and square elements.

To demonstrate the flexibility of the HNI method, as an alternative to the near-tip functions in (11c), we consider *vectorial* enrichment functions [23]. This enrichment strategy reduces the number of degrees of freedom that are needed to capture the asymptotic behavior of the displacement field near the crack tip and also improves the condition number of the stiffness matrix [24]. The X-FEM displacement field with vectorial enrichment for an edge crack is:

$$\boldsymbol{u}_e^h(\boldsymbol{x}) = \sum_{i\in\mathbb{I}} N_i(\boldsymbol{x})\boldsymbol{u}_i + \sum_{j\in\mathbb{J}\subseteq\mathbb{I}} N_j(\boldsymbol{x})H(\boldsymbol{x})\boldsymbol{a}_j + \sum_{k\in\mathbb{K}\subseteq\mathbb{I}} N_k(\boldsymbol{x})\sum_{\alpha=1}^{2}\boldsymbol{k}_\alpha(\boldsymbol{x})b_{k\alpha}, \tag{17a}$$

Prepared using nmeauth.cls
DOI: 10.1002/nme

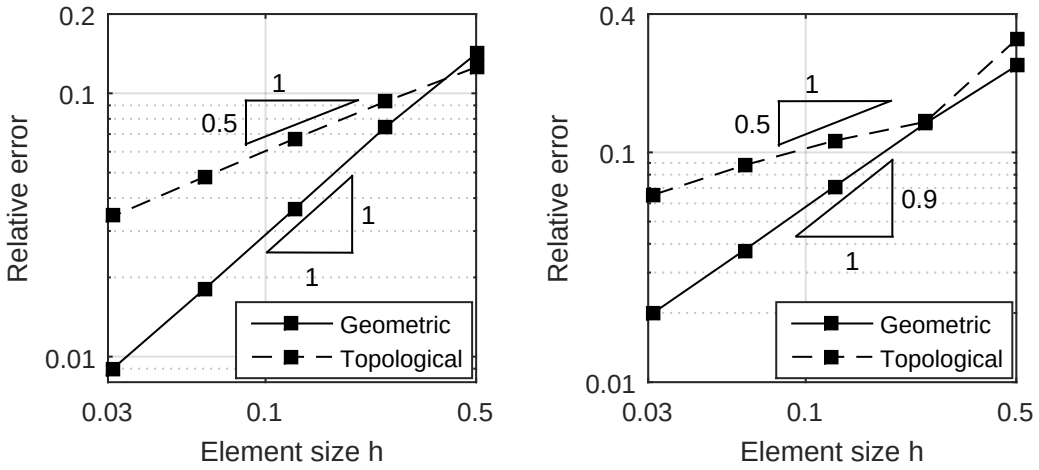

Figure 13. Convergence in the energy seminorm for the edge-crack problem using (a) rectangular and (b) triangular meshes. Rates of convergence of 1/2 (suboptimal) for topological enrichment and 1 (optimal) for geometric enrichment are obtained.

where

$$\frac{K_I}{\mu\sqrt{2\pi}}\boldsymbol{k}_1 = u_x^I\boldsymbol{i} + u_y^I\boldsymbol{j}, \quad \frac{K_{II}}{\mu\sqrt{2\pi}}\boldsymbol{k}_2 = u_x^{II}\boldsymbol{i} + u_y^{II}\boldsymbol{j}. \tag{17b}$$

In (17), $\boldsymbol{u}^I \equiv (u_x^I, u_y^I)$ and $\boldsymbol{u}^{II} \equiv (u_x^{II}, u_y^{II})$ are the pure mode I and pure mode II plane strain displacement fields, respectively (see Table I).

First, we verify for the edge-cracked problem that vectorial enrichments are able to reproduce an imposed pure mode I ($K_I = 1$) displacement field. To this end, all nodes are enriched with vectorial enrichment ($\mathbb{K} = \mathbb{I}$ and $\mathbb{J} = \emptyset$) and to exactly impose the essential boundary conditions, the coefficients associated with nodes on the boundary are set as: $\boldsymbol{u}_i = \boldsymbol{0}$, $b_{i1} = 1/(\mu\sqrt{2\pi})$, $b_{i2} = 0$. A regular 4×4 mesh is used in this study (Figure 14a). The crack tip is perturbed so that it does not coincide with a nodal location. This dramatically increases the number of cubature points that is required in the adaptive HNI rule. The crack is defined through the matrix

$$\boldsymbol{C} = \begin{bmatrix} 0 & 2.5 \\ 2.49 & 2.5 \end{bmatrix}. \tag{18}$$

Prepared using nmeauth.cls
DOI: 10.1002/nme

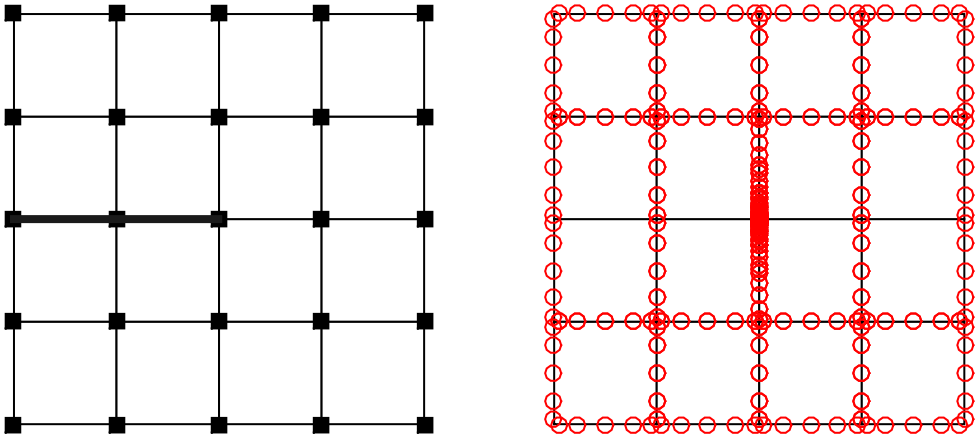

(a) (b)

Figure 14. Patch test for pure mode I displacement field. (a) Regular 4×4 mesh. Domain is $[0, 5]^2$ and the crack tip is located at $(2.49, 2.5)$. All nodes are enriched with vectorial enrichment functions; and (b) Distribution of cubature points for $tol = 10^{-5}$.

The value of *tol* in the adaptive HNI method is varied to determine its effect on the relative error. The results are listed in Table II. We observe that *tol* is strongly correlated to the relative error, which is in agreement with the study in Section 4.2. Accurate numerical integration is needed to ensure that the patch test is passed.

Now, we use near-tip and vectorial enrichment functions to perform a convergence study for the edge-cracked plate problem. Seven different meshes with varying levels of refinement are selected. On all meshes, we apply geometric enrichment with a radius of 0.7. Vertices of the crack are given in (16). A sample mesh is illustrated in Figure 15a. In Figure 15b, results for the X-FEM with vectorial and near-tip enrichments are compared. Both enrichment methods provide near-optimal rates of convergence. Near-tip enrichment delivers better accuracy at the expense of a worse condition number. For the mesh shown in Figure 15a, vectorial

Table II. Relative energy seminorm of the error as a function of the tolerance in the adaptive scheme.

tol	No. of cubature points	E_{rel}
10^{-2}	240	6.0×10^{-03}
10^{-5}	420	5.4×10^{-07}
10^{-10}	1140	1.6×10^{-09}
10^{-13}	1720	2.5×10^{-12}

Prepared using nmeauth.cls
DOI: 10.1002/nme

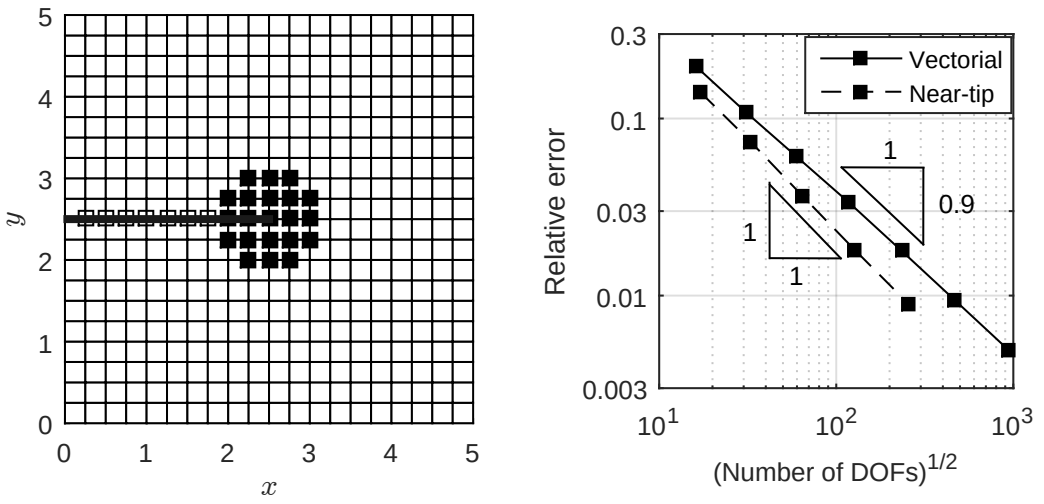

(a) (b)

Figure 15. Vectorial enrichment versus near-tip enrichment for the edge-crack problem. In (a), nodes that are enriched with near-tip/vectorial enrichment are shown as filled squares. (b) Convergence in the energy seminorm versus the square root of the number of degrees of freedom.

enrichment results in a condition number of $\mathcal{O}(10^4)$ for the stiffness matrix, whereas for near-tip enrichment, the condition number of the stiffness matrix is $\mathcal{O}(10^7)$.

5.2. Center-cracked plate

We consider the problem of a center-cracked panel subjected to a biaxial load, which was solved in Mousavi and Sukumar [8]. The problem setup is illustrated in Figure 16a. To approximate the infinite plate problem, $a/w = 0.1$ is chosen, where $2a$ is the crack width and $2w$ is the plate width and height. In the numerical computations, we choose $a = 0.25$ and use a 50×50 finite element mesh. Nine extended finite element analyses using topological enrichment are conducted for a crack that is inclined at angles $\beta = 0, \pi/16, \ldots, 7\pi/16, \pi/2$. The exact stress intensity factors for a crack in an infinite plate are [25]

$$\begin{aligned} K_I &= \sqrt{\pi a}\left(\sigma_2 \sin^2\beta + \sigma_1 \cos^2\beta\right), \\ K_{II} &= \sqrt{\pi a}\,(\sigma_2 - \sigma_1)\sin\beta\cos\beta. \end{aligned} \tag{19}$$

Analytical results from (19) and those obtained using the X-FEM are listed in Table III, and are also compared in Figure 16b. For all angles tested, SIFs from the X-FEM are less than 1 percent in error for both K_I and K_{II}.

Prepared using nmeauth.cls
DOI: 10.1002/nme

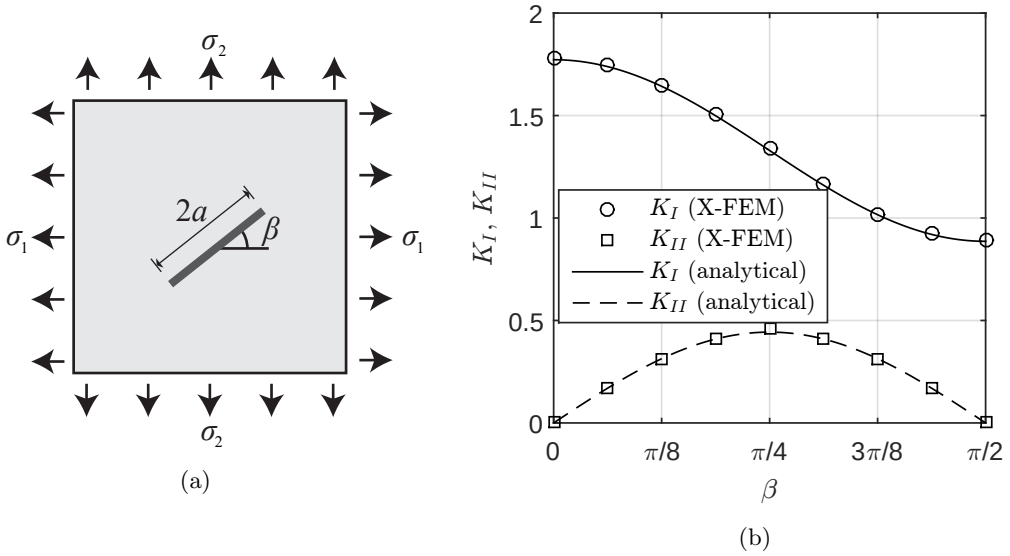

Figure 16. Inclined crack problem in a finite plate. (a) Specimen and crack dimensions, and loading. The applied tractions are: $\sigma_1 = 1$ and $\sigma_2 = 2$. (b) Comparison of SIFs from the X-FEM to the analytical results. For the X-FEM, $a/w = 0.1$, where $2w$ is the plate width.

To assess the error in modeling the infinite domain problem using a finite plate, we conduct an explicit flaw analysis on a highly-refined mesh in Abaqus for the center-crack problem ($\beta = 0$). The finite element mesh consists of eight-node quadrilateral elements, with collapsed quarter-point elements at the crack tip [26]. From the Abaqus analysis, a converged result of $K_I = 1.7971$ is obtained. In comparison, the X-FEM produces $K_I = 1.7836$ and the analytical result is $K_I = 1.7725$. The SIF from the X-FEM is about midway between the analytical and Abaqus result, and therefore if the Abaqus solution is used as the reference result in Table III, then the computed relative errors are not likely to change appreciably. With mesh refinement, stress intensity factors for $\beta = 0$ from the X-FEM converge to the Abaqus solution.

5.3. Embedded piecewise affine crack in a plate

A piecewise affine crack within a square plate that occupies the domain $\Omega = [0, 5]^2$ is considered. The crack has two kinks, and is composed of three line segments. The crack is

Prepared using nmeauth.cls
DOI: 10.1002/nme

Table III. Mixed-mode stress intensity factors for the inclined crack problem.

β	K_I (X-FEM)	K_I (analytic)	K_{II} (X-FEM)	K_{II} (analytic)
0	1.7836	1.7725	0.0000	0.0000
$\pi/16$	1.7444	1.7387	0.1700	0.1696
$\pi/8$	1.6484	1.6427	0.3136	0.3133
$3\pi/16$	1.5055	1.4989	0.4128	0.4094
$\pi/4$	1.3332	1.3293	0.4455	0.4431
$5\pi/16$	1.1642	1.1598	0.4111	0.4094
$3\pi/8$	1.0197	1.0160	0.3152	0.3133
$7\pi/16$	0.9229	0.9200	0.1692	0.1696
$\pi/2$	0.8915	0.8862	0.0000	0.0000

represented by its vertices that are stored in the matrix

$$\boldsymbol{C} = \begin{bmatrix} 1.21 & 1.28 \\ 1.73 & 2.14 \\ 2.90 & 2.71 \\ 3.56 & 3.59 \end{bmatrix}$$

and is illustrated in Figure 17a. Unit tractions are imposed in the y-direction on edges $y = 0$ and $y = 5$. The crack tips are labeled as A and B in Figure 17a. This example demonstrates the use of HNI for modeling kinked discontinuities, and hence renders it suitable for quasi-static crack growth simulations. Two separate analyses are conducted to compute the mixed-mode stress intensity factors. First, a refined explicit flaw analysis in Abaqus is used to determine converged values of K_I and K_{II} for this problem. Then, the same kinked crack is analyzed using X-FEM on refined rectangular meshes. The converged mixed-mode SIFs from Abaqus at crack-tip A are: $K_I = 1.1983$ and $K_{II} = 1.8296$. At crack-tip B, they are: $K_I = 1.4434$ and $K_{II} = 1.7362$. To generate these results, focused meshes at the crack tips are used; one of the meshes in the vicinity of crack tip B is shown in Figure 17b.

The problem is solved using the X-FEM with both topological and geometric enrichment. For geometric enrichment, the enrichment radius is set to 0.7. Five meshes are chosen whose element sizes vary from $h = 0.5$ to $h = 0.03125$. Using the Abaqus solution as the reference, the error in the mixed-mode SIFs are plotted in Figure 18. Data points with relative error of less than 10^{-4} are not shown in Figure 18. At both crack-tip A and B, we observe convergence

Prepared using nmeauth.cls
DOI: 10.1002/nme

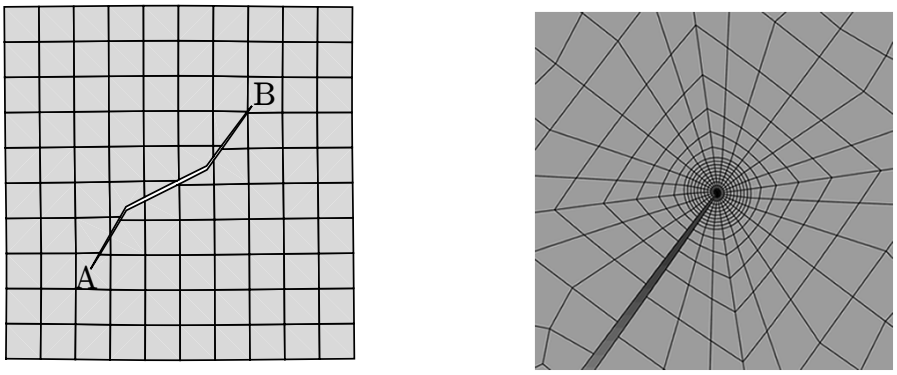

(a) (b)

Figure 17. Doubly-kinked crack in a finite plate. (a) Deformed shape obtained from X-FEM; and (b) Abaqus solution in the vicinity of crack-tip B. Deformation scale factor is 10000.

rates of at least 2 (optimal) for geometric enrichment and convergence rates of at least 1 for topological enrichment in both K_I and K_{II}. Figure 18 reveals that with geometric enrichment, a mesh with $h = 0.25$ (1312 degrees of freedom) delivers SIFs that are accurate to within one percent. In contrast, the Abaqus mesh shown in Figure 17b has 7842 degrees of freedom. However, it is possible to tailor a mesh within Abaqus for this problem that delivers the same accuracy with fewer degrees of freedom. Such optimized meshes for each crack geometry take considerable effort and time to generate, whereas a simple, structured mesh suffices for the X-FEM.

6. CONCLUDING REMARKS

In this paper, we applied a method for the numerical integration of homogeneous functions [16] (coined herein as HNI) to the problem of integrating discontinuous polynomials and weakly singular functions in the extended finite element method (X-FEM). On using HNI, polynomials are exactly integrated, and weakly singular functions are integrated to a user-specified precision using an adaptive scheme. We described the implementation of the HNI scheme to compute the element stiffness matrix and the M-integral to extract stress intensity factors. Compared to current methods for numerical integration in the X-FEM, HNI provides fast, accurate and robust integration and is the first approach that does not require element-partitioning. For elements with enriched degrees-of-freedom, the new method requires such elements in the

Prepared using nmeauth.cls
DOI: 10.1002/nme

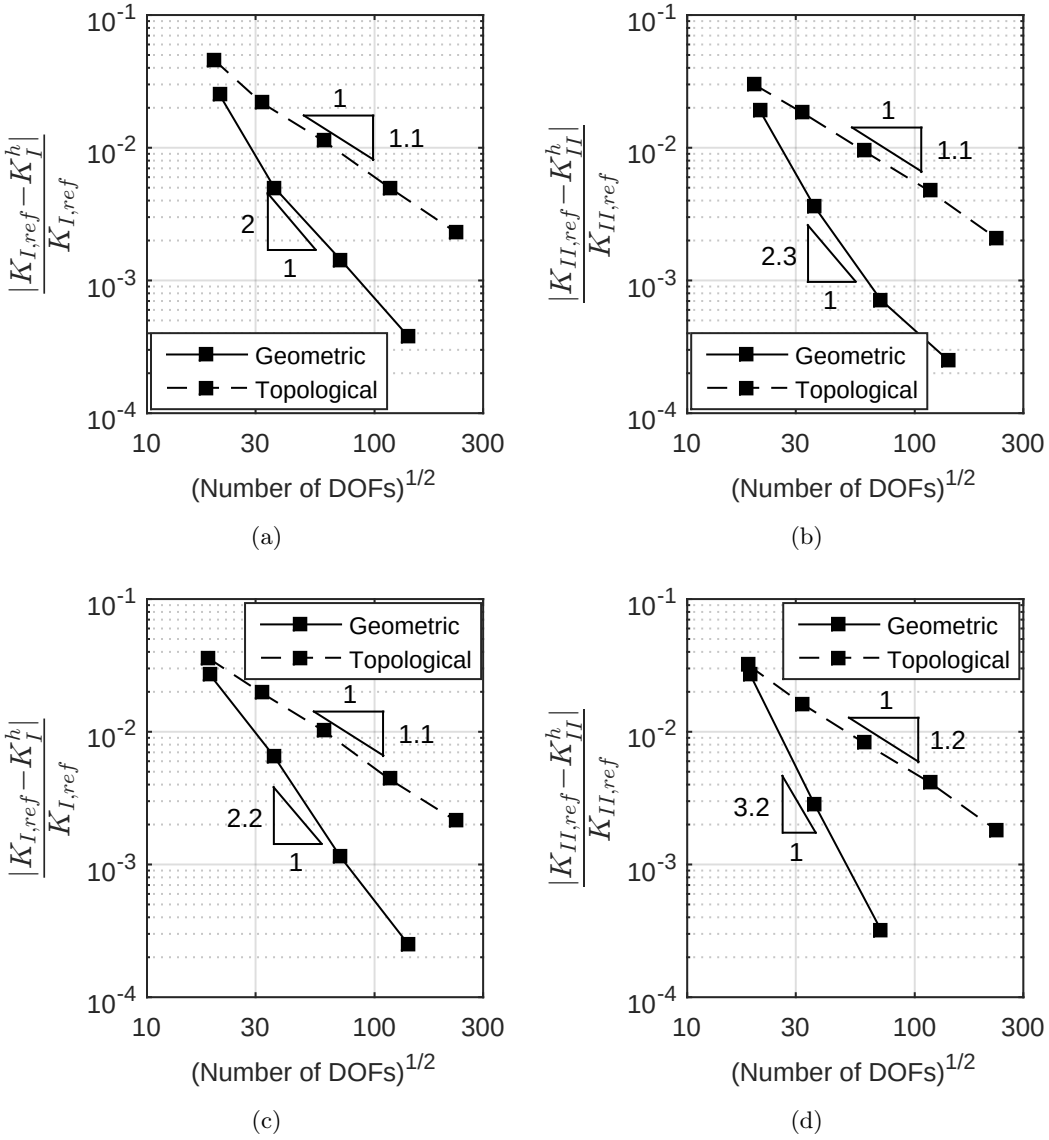

Figure 18. Convergence of SIFs for the doubly-kinked crack problem. (a) K_I at tip A; (b) K_{II} at tip A; (c) K_I at tip B; and (d) K_{II} at tip B. Geometric and topological enrichment methods are used. The Abaqus solution for the SIFs is used as the reference.

finite element mesh to have constant Jacobian in the isoparametric map. This requirement is met by unstructured Delaunay triangles and structured rectangular elements. The non-enriched elements in the mesh can consist of unstructured triangular or quadrilateral elements. We performed a detailed study on the accuracy of the stiffness matrix entries, and considered *geometric* and *topological* enrichment strategies for crack problems. We solved three benchmark crack problems, and demonstrated that the integration scheme delivered optimal rates of

Prepared using nmeauth.cls
DOI: 10.1002/nme

convergence (geometric enrichment) and excellent accuracy in SIF computations for both straight and kinked cracks.

The main advantages of using HNI for discontinuous and weakly singular integrands are eliminating the need for element-partitioning in the X-FEM (other than at crack locations) and providing very accurate and efficient integration of weakly singular functions when compared to existing methods. Since partitioning complicates coding, requires additional data structures, and can also incur overhead on the time required to conduct numerical integration, removing this need directly reduces computational demands on analysis. When compared to the generalized Duffy transformation, a singularity-canceling method for integrating weakly singular functions, the HNI method delivers accuracy that is several orders of magnitude better with far fewer cubature points. The HNI scheme also provides a means to fine-tune the cubature rule based on a user-specified level of accuracy in the integration — a feature that is not possible with singularity-canceling methods and Gauss cubature. Taken together, HNI provides fast, accurate numerical integration that enhances the robustness of the X-FEM.

The focus in this paper was on a new approach for the numerical integration of enriched basis functions for two-dimensional crack problems using the extended finite element method. The application of the HNI method naturally extends to three-dimensional cracks that are defined as the union of piecewise planar facets. In 3D, integration of discontinuous functions in Heaviside-enriched elements can be reduced to line integrals (one-dimensional Gauss quadrature rule suffices) along the edges of the facets or reduced even further to just vertex evaluations using methods described in Chin et al. [16], thereby in both cases eliminating the need for element-partitioning. HNI also simplifies integration within near-tip enriched 3D elements, though partitioning would still be required on the 2D planar facets. In this paper, we investigated the use of HNI for crack problems with the X-FEM, though as noted in Chin et al. [16], the HNI approach has broader appeal. In addition to crack problems, it is well-suited for many other applications of the X-FEM as well as other emerging computational methods that require numerical integration of discontinuous and/or weakly singular functions over convex and nonconvex regions. As a next step, we intend to apply the HNI scheme to model weak discontinuities (affine and curved material interfaces) with the extended finite element method.

Prepared using nmeauth.cls
DOI: 10.1002/nme

A. HOMOGENEOUS SHAPE FUNCTIONS AND THEIR DERIVATIVES

In this appendix, we consider two finite elements that are compatible with the HNI method: the linear triangle and the bilinear rectangle. Shape functions for these elements are polynomial and known in closed-form in global coordinates, allowing them to be written as a collections of homogeneous functions. In this section, homogenized versions of the element shape functions and their derivatives are presented for use with the HNI approach. The notation $f^{[q]}$ is used to denote that the function f is homogeneous of degree q.

Computing quantities in local crack-tip coordinates requires a mapping between the global coordinate system and the local coordinate system. This mapping is given by

$$\hat{\boldsymbol{x}} = \hat{\boldsymbol{x}}(\boldsymbol{x}) = \boldsymbol{R}(\boldsymbol{x} - \boldsymbol{c}_1), \tag{20}$$

where $\hat{\boldsymbol{x}} \equiv (\hat{x}, \hat{y})$ is the local crack-tip coordinate, $\boldsymbol{c}_1$ (or $\boldsymbol{c}_{n_c}$) $\equiv (x_c, y_c)$ is the location of the crack tip, and $\boldsymbol{R} := \boldsymbol{R}(\phi)$ is the rotation matrix for an angle ϕ that represents the angle of inclination of the crack. The inverse map is:

$$\boldsymbol{x} = \boldsymbol{x}(\hat{\boldsymbol{x}}) = \boldsymbol{R}^T\hat{\boldsymbol{x}} + \boldsymbol{c}_1 = \hat{\boldsymbol{x}}_r + \boldsymbol{c}_1, \quad \hat{\boldsymbol{x}}_r := \boldsymbol{R}^T\hat{\boldsymbol{x}}. \tag{21}$$

Note that (20) and (21) are not homogeneous, leading to different homogenized functions for the shape function derivatives in crack-tip coordinates versus global coordinates.

A.1. Linear triangle

A linear triangular finite element is shown in Figure 19a. The nodal coordinates for this element are: (x_1, y_1), (x_2, y_2), and (x_3, y_3) for nodes 1, 2, and 3, respectively. The shape functions are:

$$\begin{aligned}
N_1(\boldsymbol{x}) &= \left[(x_2y_3 - x_3y_2) + (y_2 - y_3)x + (x_3 - x_2)y\right]/A_e, \\
N_2(\boldsymbol{x}) &= \left[(x_3y_1 - x_1y_3) + (y_3 - y_1)x + (x_1 - x_3)y\right]/A_e, \\
N_3(\boldsymbol{x}) &= \left[(x_1y_2 - x_2y_1) + (y_1 - y_2)x + (x_2 - x_1)y\right]/A_e,
\end{aligned}$$

where $N_i(\boldsymbol{x})$ is the shape function for node i and A_e is the area of the triangle.

Prepared using nmeauth.cls
DOI: 10.1002/nme

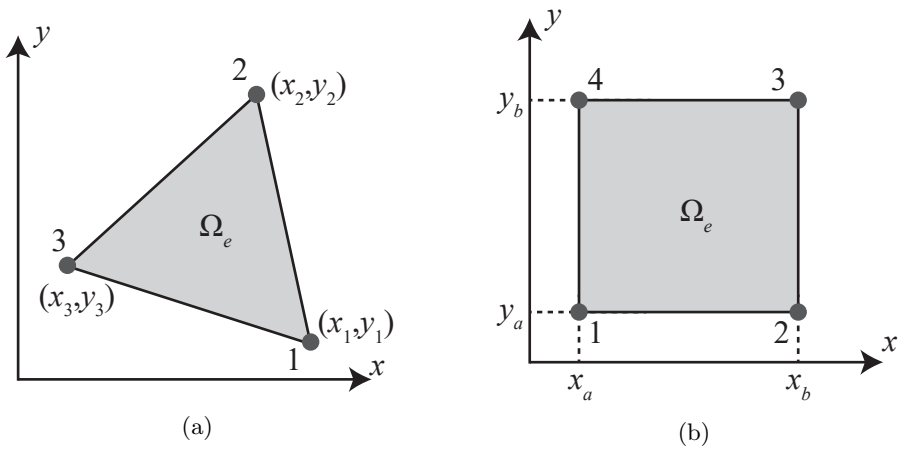

Figure 19. (a) Linear triangular finite element; and (b) Bilinear rectangular finite element.

Table IV. Shape functions homogenized in local crack-tip coordinates for the triangular finite element.

i	q	$N_i^{[q]}(\hat{\boldsymbol{x}})$
1	0	$\dfrac{(x_2y_3 - x_3y_2) + (y_2 - y_3)x_c + (x_3 - x_2)y_c}{A_e}$
	1	$\dfrac{(y_2 - y_3)\hat{x}_r + (x_3 - x_2)\hat{y}_r}{A_e}$
2	0	$\dfrac{(x_3y_1 - x_1y_3) + (y_3 - y_1)x_c + (x_1 - x_3)y_c}{A_e}$
	1	$\dfrac{(y_3 - y_1)\hat{x}_r + (x_1 - x_3)\hat{y}_r}{A_e}$
3	0	$\dfrac{(x_1y_2 - x_2y_1) + (y_1 - y_2)x_c + (x_2 - x_1)y_c}{A_e}$
	1	$\dfrac{(y_1 - y_2)\hat{x}_r + (x_2 - x_1)\hat{y}_r}{A_e}$

Homogeneous shape functions in local crack-tip coordinates are given in Table IV. Since shape function derivatives are constant for the linear triangle element, they are independent of the coordinate system and do not need to be homogenized. The shape function derivatives are listed in Table V.

A.2. Bilinear rectangle

The bilinear rectangular finite element is shown in Figure 19b. The nodal coordinates are: (x_a, y_a), (x_b, y_a), (x_b, y_b), and (x_a, y_b) for nodes 1, 2, 3, and 4, respectively. The finite element

Prepared using nmeauth.cls
DOI: 10.1002/nme

Table V. Shape function derivatives for the triangular finite element.

i	$N^{[0]}_{i,x}(\boldsymbol{x}) \equiv N^{[0]}_{i,x}(\hat{\boldsymbol{x}})$	$N^{[0]}_{i,y}(\boldsymbol{x}) \equiv N^{[0]}_{i,y}(\hat{\boldsymbol{x}})$
1	$\dfrac{y_2 - y_3}{A_e}$	$\dfrac{x_3 - x_2}{A_e}$
2	$\dfrac{y_3 - y_1}{A_e}$	$\dfrac{x_1 - x_3}{A_e}$
3	$\dfrac{y_1 - y_2}{A_e}$	$\dfrac{x_2 - x_1}{A_e}$

Table VI. Shape functions homogenized in local crack-tip coordinates for the rectangular finite element.

i	$N^{[0]}_i(\hat{\boldsymbol{x}})$	$N^{[1]}_i(\hat{\boldsymbol{x}})$	$N^{[2]}_i(\hat{\boldsymbol{x}})$
1	$+\dfrac{x'_b y'_b}{A_e}$	$-\dfrac{(y'_b \hat{x}_r + x'_b \hat{y}_r)}{A_e}$	$+\dfrac{\hat{x}_r \hat{y}_r}{A_e}$
2	$-\dfrac{x'_a y'_b}{A_e}$	$+\dfrac{(y'_b \hat{x}_r + x'_a \hat{y}_r)}{A_e}$	$-\dfrac{\hat{x}_r \hat{y}_r}{A_e}$
3	$+\dfrac{x'_a y'_a}{A_e}$	$-\dfrac{(y'_a \hat{x}_r + x'_a \hat{y}_r)}{A_e}$	$+\dfrac{\hat{x}_r \hat{y}_r}{A_e}$
4	$-\dfrac{x'_b y'_a}{A_e}$	$+\dfrac{(y'_a \hat{x}_r + x'_b \hat{y}_r)}{A_e}$	$-\dfrac{\hat{x}_r \hat{y}_r}{A_e}$

shape functions are:

$$N_1(\boldsymbol{x}) = (x_b - x)(y_b - y)/A_e, \qquad N_2(\boldsymbol{x}) = (x - x_a)(y_b - y)/A_e,$$
$$N_3(\boldsymbol{x}) = (x - x_a)(y - y_a)/A_e, \qquad N_4(\boldsymbol{x}) = (x_b - x)(y - y_a)/A_e,$$

where $A_e = (x_b - x_a)(y_b - y_a)$ is the area of the rectangle.

Homogeneous shape functions in local crack-tip coordinates are given in Table VI. Table VII provides shape function derivatives homogenized with respect to local crack-tip coordinates, and Table VIII lists the same derivatives homogenized with respect to global coordinates. In these tables, we make use of the following definitions: $\boldsymbol{x}'_a := \boldsymbol{x}_a - \boldsymbol{c}_1$ and $\boldsymbol{x}'_b := \boldsymbol{x}_b - \boldsymbol{c}_1$.

ACKNOWLEDGEMENT

The authors gratefully acknowledge the research support of the National Science Foundation through contract grant CMMI-1334783 to the University of California at Davis.

Prepared using nmeauth.cls
DOI: 10.1002/nme

Table VII. Shape function derivatives homogenized with respect to local crack-tip coordinates for the rectangular finite element.

i	$N^{[0]}_{i,x}(\hat{\boldsymbol{x}})$	$N^{[1]}_{i,x}(\hat{\boldsymbol{x}})$	$N^{[0]}_{i,y}(\hat{\boldsymbol{x}})$	$N^{[1]}_{i,y}(\hat{\boldsymbol{x}})$
1	$-\frac{y'_b}{A_e}$	$+\frac{\hat{y}_r}{A_e}$	$-\frac{x'_b}{A_e}$	$+\frac{\hat{x}_r}{A_e}$
2	$+\frac{y'_b}{A_e}$	$-\frac{\hat{y}_r}{A_e}$	$+\frac{x'_a}{A_e}$	$-\frac{\hat{x}_r}{A_e}$
3	$-\frac{y'_a}{A_e}$	$+\frac{\hat{y}_r}{A_e}$	$-\frac{x'_a}{A_e}$	$+\frac{\hat{x}_r}{A_e}$
4	$+\frac{y'_a}{A_e}$	$-\frac{\hat{y}_r}{A_e}$	$+\frac{x'_b}{A_e}$	$-\frac{\hat{x}_r}{A_e}$

Table VIII. Shape function derivatives homogenized with respect to global coordinates for the rectangular finite element.

i	$N^{[0]}_{i,x}(\boldsymbol{x})$	$N^{[1]}_{i,x}(\boldsymbol{x})$	$N^{[0]}_{i,y}(\boldsymbol{x})$	$N^{[1]}_{i,y}(\boldsymbol{x})$
1	$-\frac{y_b}{A_e}$	$+\frac{y}{A_e}$	$-\frac{x_b}{A_e}$	$+\frac{x}{A_e}$
2	$+\frac{y_b}{A_e}$	$-\frac{y}{A_e}$	$+\frac{x_a}{A_e}$	$-\frac{x}{A_e}$
3	$-\frac{y_a}{A_e}$	$+\frac{y}{A_e}$	$-\frac{x_a}{A_e}$	$+\frac{x}{A_e}$
4	$+\frac{y_a}{A_e}$	$-\frac{y}{A_e}$	$+\frac{x_b}{A_e}$	$-\frac{x}{A_e}$

REFERENCES

1. N. Moës, J. E. Dolbow, and T. Belytschko. A finite element method for crack growth without remeshing. *International Journal for Numerical Methods in Engineering*, 46:131–150, 1999.
2. J. M. Melenk and I. Babuška. The partition of unity finite element method: Basic theory and applications. *Computer Methods in Applied Mechanics and Engineering*, 139:289–314, 1996.
3. N. Sukumar, J. E. Dolbow, and N. Moës. Extended finite element method in computational fracture mechanics: a retrospective examination. *International Journal of Fracture*, 196:189–206, 2015.
4. G. Ventura. On the elimination of quadrature subcells for discontinuous functions in the eXtended Finite-Element Method. *International Journal for Numerical Methods in Engineering*, 66(5):761–795, 2006.
5. D. J. Holdych, D. R. Noble, and R. B. Secor. Quadrature rules for triangular and tetrahedral elements with generalized functions. *International Journal for Numerical Methods in Engineering*, 73(9):1310–1327, 2008.
6. G. Ventura and E. Benvenuti. Equivalent polynomials for quadrature in Heaviside function enriched elements. *International Journal for Numerical Methods in Engineering*, 102(3–4):688–710, 2015.
7. S. Natarajan, D. R. Mahapatra, and S. P. A. Bordas. Integrating strong and weak discontinuities without integration subcells and example applications in an XFEM/GFEM framework. *International Journal for Numerical Methods in Engineering*, 83(3):269–294, 2010.

Prepared using nmeauth.cls
DOI: 10.1002/nme

8. S. E. Mousavi and N. Sukumar. Generalized Gaussian quadrature rules for discontinuities and crack singularities in the extended finite element method. *Computer Methods in Applied Mechanics and Engineering*, 199(49):3237–3249, 2010.
9. J. B. Lasserre. Integration on a convex polytope. *Proceedings of the American Mathematical Society*, 126(8):2433–2441, 1998.
10. Y. Sudhakar and W. A. Wall. Quadrature schemes for arbitrary convex/concave volumes and integration of weak form in enriched partition of unity methods. *Computer Methods in Applied Mechanics and Engineering*, 258:39–54, 2013.
11. E. Béchet, H. Minnebo, N. Moës, and B. Burgardt. Improved implementation and robustness study of the X-FEM for stress analysis around cracks. *International Journal for Numerical Methods in Engineering*, 64(8):1033–1056, 2005.
12. P. Laborde, J. Pommier, Y. Renard, and M. Salaün. High-order extended finite element method for cracked domains. *International Journal for Numerical Methods in Engineering*, 64(3):354–381, 2005.
13. M. G. Duffy. Quadrature over a pyramid or cube of integrands with a singularity at a vertex. *SIAM Journal on Numerical Analysis*, 19(6):1260–1262, 1982.
14. S. E. Mousavi and N. Sukumar. Generalized Duffy transformation for integrating vertex singularities. *Computational Mechanics*, 45(2–3):127–140, 2010.
15. A. Cano and C. Moreno. A new method for numerical integration of singular functions on the plane. *Numerical Algorithms*, 68(3):547–568, 2015.
16. E. B. Chin, J. B. Lasserre, and N. Sukumar. Numerical integration of homogeneous functions on convex and nonconvex polygons and polyhedra. *Computational Mechanics*, 56(6):967–981, 2015.
17. J. B. Lasserre. Integration and homogeneous functions. *Proceedings of the American Mathematical Society*, 127(3):813–818, 1999.
18. Dassault Systèmes Simulia Corporation. *Abaqus Analysis User's Guide*, 2013. Version 6.13-1.
19. C. P. Simon and L. E. Blume. *Mathematics for Economists*. W. W. Norton and Company, New York, 1994.
20. M. E. Taylor. *Partial Differential Equations: Basic Theory*. Springer-Verlag, New York, 1996.
21. J. F. Yau, S. S. Wang, and H. T. Corten. A mixed-mode crack analysis of isotropic solids using conservation laws of elasticity. *Journal of Applied Mechanics*, 47(2):335–341, 1980.
22. B. Moran and C. F. Shih. Crack tip and associated domain integrals from momentum and energy balance. *Engineering Fracture Mechanics*, 27(6):615–642, 1987.
23. C. A. M. Duarte, I. Babuška, and J. T. Oden. Generalized finite element methods for three dimensional structural mechanics problems. *Computers and Structures*, 77(2):215–232, 2000.
24. N. Chevaugeon, N. Moës, and H. Minnebo. Improved crack tip enrichment functions and integration for crack modeling using the extended finite element method. *International Journal for Multiscale Computational Engineering*, 11(6):597–631, 2013.
25. M. H. Aliabadi, D. P. Rooke, and D. J. Cartwright. Mixed-mode Bueckner weight functions using boundary element analysis. *International Journal of Fracture*, 34(2):131–147, 1987.
26. R. S. Barsoum. On the use of isoparametric finite elements in linear fracture mechanics. *International Journal of Fracture*, 10(1):25–37, 1976.

DOI: 10.1002/nme